

Spin-Orbit Coupled Insulators and Metals on the Verge of Kitaev Spin Liquids in Ilmenite Heterostructures

Yi-Feng Zhao,^{1,*} Seong-Hoon Jang,² and Yukitoshi Motome^{1,†}

¹*Department of Applied Physics, University of Tokyo, Bunkyo, Tokyo 113-8656, Japan*

²*Institute for Materials Research, Tohoku University, Aoba, Sendai, 980-8577, Japan*

Competition and cooperation between electron correlation and relativistic spin-orbit coupling give rise to diverse exotic quantum phenomena in solids. An illustrative example is spin-orbit entangled quantum liquids, which exhibit remarkable features such as topological orders and fractional excitations. The Kitaev honeycomb model realizes such interesting states, called the Kitaev spin liquids, but its experimental feasibility is still challenging. Here we theoretically investigate hexagonal heterostructures including a candidate for the Kitaev magnets, an ilmenite oxide MgIrO_3 , to actively manipulate the electronic and magnetic properties toward the realization of the Kitaev spin liquids. For three different structure types of ilmenite bilayers $\text{MgIrO}_3/A\text{TiO}_3$ with $A = \text{Mn, Fe, Co, and Ni}$, we obtain the optimized lattice structures, the electronic band structures, the stable magnetic orders, and the effective magnetic couplings, by combining *ab initio* calculations and the effective model approaches. We find that the spin-orbital coupled bands characterized by the pseudospin $j_{\text{eff}} = 1/2$, crucially important for the Kitaev-type interactions, are retained in the MgIrO_3 layer for all the heterostructures, but the magnetic state and the band gap depend on the types of heterostructures as well as the A atoms. In particular, one type becomes metallic irrespective of A , while the other two are mostly insulating. We show that the insulating cases provide spin-orbit coupled Mott insulating states with dominant Kitaev-type interactions, accompanied by different combinations of subdominant interactions depending on the heterostructural type and A , while the metallic cases realize spin-orbit coupled metals with various doping rates. Our results indicate that these hexagonal heterostructures are a good platform for engineering electronic and magnetic properties of the spin-orbital coupled correlated materials, including the possibility of Majorana Fermi surfaces and topological superconductivity.

I. INTRODUCTION

Strong electron correlations, represented as Coulomb repulsion U , play a pivotal role in $3d$ transition metal compounds and lead to a plethora of intriguing phenomena, such as the Mott transition and high-temperature superconductivity [1, 2]. The other key concept of quantum materials, the spin-orbit coupling (SOC), represented as λ , is a relativistic effect entangling the spin degree of freedom and the orbital motion of electrons, which is an essential ingredient in the topological insulators [3, 4]. Beyond their independent effects, synergy between U and λ has attracted increasing attention recently due to the emergence of new states of matter, such as axion insulators [5, 6] and topological semimetals [7–9]. In general, it is difficult for the SOC to dramatically influence the electronic properties in $3d$ transition metal compounds since λ is much smaller than U . However, when proceeding to $4d$ and $5d$ systems, the d orbitals are spatially more spread out, which reduces U , and at the same time, the relativistic effect becomes larger for heavier atoms, enhancing λ . Hence, in these systems, the competition and cooperation between U and λ play a decisive role in their electronic states and allow us to access the intriguing regime that yields the exotic correlated states of matter [10].

One of the striking examples is the spin-orbit coupled Mott insulator, typically realized in the iridium oxides with Ir^{4+} valence, e.g., Sr_2IrO_4 [11, 12]. In each Ir ion located in the center of the IrO_6 octahedron, the crystal field energy, which is significantly larger than U and λ , splits the d orbital manifold into low-energy t_{2g} and high-energy e_g ones. For Sr_2IrO_4 , five electrons occupy the t_{2g} orbitals and make the system yield the t_{2g}^5 low-spin state. Usually, the partially-filled orbital causes a metallic state according to the conventional band theory, but the insulating state was observed in experiments [13]. Considering the large SOC, the t_{2g} manifold continues to split into high-energy doublet characterized with the pseudospin $j_{\text{eff}} = 1/2$ and low-energy quartet with $j_{\text{eff}} = 3/2$; the latter is fully occupied and the former is half filled. Finally, a Mott gap is opened in the half-filled $j_{\text{eff}} = 1/2$ band by U . This accounts for the insulating nature of the system, and the Mott insulating state realized in the spin-orbital coupled bands is called the spin-orbit coupled Mott insulator.

The quantum spin liquid (QSL), one of the most exotic quantum states in the spin-orbit coupled Mott insulators, has received increasing attention due to the emergence of remarkable properties, e.g., fractional excitations [14] and topological orders [15]. In the QSL, long-range magnetic ordering is suppressed down to zero temperature due to strong quantum fluctuations, though the localized magnetic moments are quantum entangled [16–19]. The presence of fractional quasiparticles that obey the non-abelian statistics is not only of great fundamental phys-

* zyf@g.ecc.u-tokyo.ac.jp

† motome@ap.t.u-tokyo.ac.jp

ical research, but also promising toward quantum computation [20]. In general, one route to realizing the QSL depends on geometrical frustration. Indeed, experiments have evidenced several candidates of QSL in antiferromagnets with lattice structures including triangular unit, where magnetic frustration is the common feature [21–23]. The other route to the QSL is the so-called exchange frustration caused by the conflicting constraints between anisotropic exchange interactions [24]. The strong spin-orbital entanglement in the spin-orbit coupled Mott insulators, in general, gives rise to spin anisotropy, offering a good playground for the exchange frustration, even on the lattices without geometrical frustration.

The Kitaev model is a distinctive quantum spin model realizing the exchange frustration [25]. The model is defined for $S = \frac{1}{2}$ local magnetic moments on the two-dimensional (2D) honeycomb lattice with the Ising-type bond-dependent anisotropic interactions, whose Hamiltonian is given by

$$\mathcal{H} = \sum_{\alpha} \sum_{\langle i,j \rangle_{\alpha}} K_{\alpha} S_i^{\alpha} S_j^{\alpha}, \quad (1)$$

where $\alpha = x, y, z$ denote the three bonds of the honeycomb lattice, and K_{α} is the exchange coupling constant on the α bond; the sum of $\langle i, j \rangle_{\alpha}$ is taken for nearest-neighbor sites of i and j on the α bonds. In this model, the orthogonal anisotropies on the x, y, z bonds provide the exchange frustration. Importantly, the model is exactly solvable, and the ground state is a QSL with fractional excitations, itinerant Majorana fermions and localized Z_2 fluxes [25]. Moreover, the anyonic excitations in this model hold promise for applications in quantum computing [25, 26]; especially, non-Abelian anyons, which follow braiding rules similar to those of conformal blocks for the Ising model, appear under an external magnetic field.

The exchange frustration in the Kitaev-type interactions can be realized in real materials when two conditions are met [27]. First, at each magnetic ion, the spin-orbit coupled Mott insulating state with pseudospin $j_{\text{eff}} = 1/2$ should be realized. Second, the pseudospins need to interact with each other through the ligands shared by neighboring octahedra which forms edge-sharing network. Over the past decade, enormous efforts have been devoted to exploring the candidate materials for the Kitaev QSL that meet these conditions [28–31]. Fortunately, dominant Kitaev-type interactions were indeed discovered in several materials, such as $A_2\text{IrO}_3$ with $A = \text{Li}$ and Na [32–38] and $\alpha\text{-RuCl}_3$ [39–46]. Not only the $5d$ and $4d$ candidates, $3d$ transition metal compounds like Co oxides have also been investigated [47, 48]. In addition to these examples with ferromagnetic (FM) Kitaev interactions, the antiferromagnetic (AFM) Kitaev QSL candidates were also predicted by *ab initio* calculations, e.g., f -electron based magnets [49, 50] and polar spin-orbit coupled Mott insulators $\alpha\text{-RuH}_{3/2}\text{X}_{3/2}$ with $X = \text{Cl}$ and Br in the Janus structure [51].

Although a plethora of Kitaev QSL candidates have been investigated, those realizing the Kitaev QSL in the

ground state are still missing, since a long-range magnetic order due to parasitic interactions such as the Heisenberg interaction hinders the Kitaev QSL. Considerable efforts have been dedicated to suppressing the parasitic interactions and/or enhancing the Kitaev-type interaction. One way is to utilize heterostructures that incorporate the Kitaev candidates. For example, the Kitaev interaction is promoted more than 50% for the heterostructure composed of 2D monolayers of $\alpha\text{-RuCl}_3$ and graphene compared to the pristine $\alpha\text{-RuCl}_3$, predicted by *ab initio* calculations [52]. The heterostructures between a 2D $\alpha\text{-RuCl}_3$ and three-dimensional (3D) topological insulator $\text{BiSbTe}_{1.5}\text{Se}_{1.5}$ evidenced the charge transfer phenomena, albeit the magnetic properties were not reported [53]. Within the realm of Kitaev heterostructures, remarkably few studies have been designed for the composite 3D/3D superlattices due to the fabrication challenge [54]. To date, few attempts [55] have been made to investigate the development of the electronic band structure and the magnetic properties, particularly whether the Kitaev interaction is still dominant when constructing the 3D/3D heterostructures using Kitaev QSL candidates.

In this paper, we theoretically study the electronic and magnetic properties in bilayer heterostructures as an interface of 3D/3D superlattices using a recently-synthesized iridium ilmenite MgIrO_3 [56] and other ilmenite magnets ATiO_3 with $A = \text{Mn}, \text{Fe}, \text{Co},$ and Ni as the substrate. This material choice is motivated by two key considerations: (i) All of these materials have been successfully synthesized in experiments, which is helpful for the epitaxial growth of multilayer heterostructures, and (ii) the ilmenite MgIrO_3 is identified as a good candidate for Kitaev magnets [57, 58]. We consider three configurations of heterostructures, classified by type-I, II, and III, which are all chemically allowed due to the characteristics of the alternative layer stacking in ilmenites, as shown in Fig. 1. The electronic band structures, magnetic ground states, and the effective exchange interactions are systematically investigated by employing the combinatorial of *ab initio* calculations, construction of the effective tight-binding model, and perturbation expansions. We find that (i) the spin-orbit coupled bands characterized by the effective pseudospin $j_{\text{eff}} = 1/2$, a key demand for Kitaev-type interactions, are still preserved in the MgIrO_3 layer for all types of the heterostructures, (ii) type-I and III heterostructures realize spin-orbit coupled Mott insulators excluding Mn type-III, whereas type-II ones are spin-orbit coupled metals with doped $j_{\text{eff}} = 1/2$ bands with various carrier concentrations, and (iii) in almost all of the insulating cases, the Kitaev-type interactions are predominant, whereas the forms and magnitudes of the other parasitic interactions depend on the specific types of the heterostructures and the A atoms.

The structure of the remaining article is as follows. In Sec. II, we provide a detailed description of the optimized lattice structures of $\text{MgIrO}_3/\text{ATiO}_3$ heterostructures with $A = \text{Mn}, \text{Fe}, \text{Co},$ and Ni . In Sec. III, we

introduce the methods employed in this work, including the means for structural optimization and the *ab initio* calculations with LDA+SOC+ U scheme (Sec. III A), the estimates of the effective transfer integral and construction of the multiorbital Hubbard model (Sec. III B), and the second-order perturbation that is used in the estimation of exchange interactions (Sec. III C). In Sec. IV, we systematically display the results of the electronic band structures for three types of heterostructure $\text{MgIrO}_3/\text{ATiO}_3$. In Sec. IV A, we present the electronic band structures for the paramagnetic state obtained by LDA+SOC, together with the projected density of states (PDOS) derived by the maximally-localized Wannier function (MLWF). In Sec. IV B, we discuss the stable magnetic states within LDA+SOC+ U and show their band structures and PDOS. In Sec. V, we derive the effective exchange coupling constants for the heterostructures for which the LDA+SOC+ U calculations suggest spin-orbit coupled Mott insulating nature, and show their location in the phase diagram for the K - J - Γ model. In Sec. VI, we discuss the possibility of the realization of Majorana Fermi surfaces (Sec. VI A) and exotic superconducting phases (Sec. VI B) in the heterostructures, and the feasibility of these heterostructures in experiments (Sec. VI C). Section VII is devoted to the summary and prospects. In Appendix A, we present the details of the energy difference of the magnetic orders and the effective exchange couplings between the A ions. We present additional information on orbital projected band structures for different specific types of heterostructures of A atoms in Appendix B and the band structures of monolayer MgIrO_3 in Appendix C.

II. HETEROSTRUCTURES

MgIrO_3 and ATiO_3 both belong to ilmenite oxides ABO_3 with $R\bar{3}$ space group. The lattice structure consists of alternative stacking of honeycomb layers with edge-sharing AO_6 octahedra and those with BO_6 octahedra. The common stacking layer structures reduce the lattice mismatch to form the heterostructures and also make them feasible to fabricate in experiments. In this study, we consider heterostructures composed of monolayer of MgIrO_3 and ATiO_3 with the balance chemical formula, to clarify the interface effect on the electronic properties of 3D/3D superlattices. Specifically, we construct three types of heterostructures, distinguished by the intersurface atoms and pertinent octahedra in the middle layer, labeled as type-I, II, and III and shown in Fig. 1. For type-I, the top and bottom layers are made of honeycomb networks of IrO_6 and TiO_6 octahedra, respectively, whereas the sandwiching honeycomb layer is formed of alternating MgO_6 and AO_6 octahedra. In the type-II, the bottom layer is replaced by AO_6 honeycomb layer, resulting in a mixture of MgO_6 and TiO_6 in the middle layer. The type-III has a similar constitution of top and bottom layers to type-I, while the middle

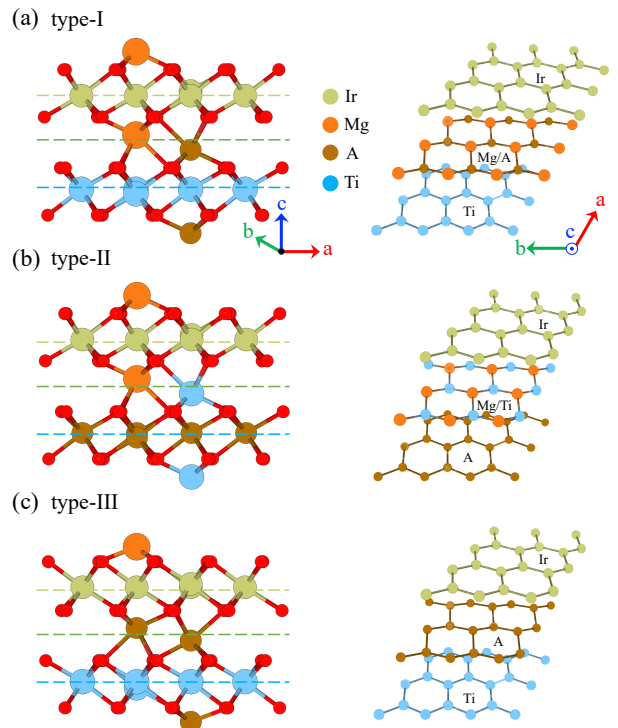


FIG. 1. Schematic pictures of crystal structures for three types of the heterostructures $\text{MgIrO}_3/\text{ATiO}_3$: (a) type-I, (b) type-II, and (c) type-III with $A = \text{Mn, Fe, Co, or Ni}$. The left and right panels show the side views and the bird's-eye views, respectively. The type-I is composed of the top honeycomb layer with edge-sharing IrO_6 octahedra and the bottom honeycomb layer of TiO_6 , sandwiching a honeycomb layer of alternating MgO_6 and AO_6 octahedra. In the type-II, the bottom is replaced by the AO_6 honeycomb layer, leaving a mixture of MgO_6 and TiO_6 in the middle, and in the type-III, the middle is replaced by the AO_6 honeycomb layer. In type-I and II, the chemical formula is commonly given by $\text{Mg}_2\text{Ir}_2\text{O}_6/\text{A}_2\text{Ti}_2\text{O}_6$, but that for type-III is $\text{MgAlr}_2\text{O}_6/\text{A}_2\text{Ti}_2\text{O}_6$. The crystal structures are embodied by VESTA [59].

layer is fully composed of AO_6 octahedra. We intentionally design these structures to balance their chemical valences and prevent the presence of redundant charges. This can be derived from the chemical formula for each type of the heterostructure, such as $\text{Mg}_2\text{Ir}_2\text{O}_6/\text{A}_2\text{Ti}_2\text{O}_6$ for type-I and II, and $\text{MgAlr}_2\text{O}_6/\text{A}_2\text{Ti}_2\text{O}_6$ for type-III, respectively.

We optimize the lattice structures of the heterostructures by the optimization scheme in Sec. III A. The information of the stable lattice structures, including the in-plane lattice constant, the bond distance between adjacent Ir atoms and O atoms, and the angle between the neighboring Ir, O, and Ir atoms, are listed in Table I for three types of the heterostructures with different A atoms. For comparison, the experimental structures of the bulk MgIrO_3 are also listed. We find all the in-plane constants are close to the bulk value of 5.158 Å, in which

the maximum and minimum lattice mismatch is 1.2% and 0.1% respectively of type-II for the Fe atom and type-III for the Mn atom. See also the discussion in Sec. VIC. Meanwhile, not only the in-plane constants but also the bond distances of Ir atoms are both enlarged as the increase of ionic radii of A atoms. The heterostructural type can significantly influence the bond distance and angle as well. For example, the angle between neighboring Ir atoms and the intermediate O atom $\theta_{\text{Ir-O-Ir}} = 96.69^\circ$ of type-II for the Ni case largely increases from that of 94.03° of the bulk case. In terms of the Ir-Ir bond length ($d_{\text{Ir-Ir}}$), the length of 2.986 Å for the bulk [56] is substantially decreased to 2.930 Å of type-II for the Fe case. Meanwhile, the Ir-O bond length $d_{\text{Ir-O}}$ of all cases are enlarged compared with that of the bulk system of 1.942 Å, in which type-III with Co atoms is maximally influenced.

TABLE I. Structural information of optimized heterostructures for $\text{MgIrO}_3/\text{ATiO}_3$ ($A = \text{Mn, Fe, Co, and Ni}$): a denotes the in-plane lattice constant, and d and θ represent the bond distance and the angle between neighboring ions, respectively. The experimental information on the bulk MgIrO_3 is also shown for comparison.

A	type	$a(\text{Å})$	$d_{\text{Ir-Ir}}(\text{Å})$	$d_{\text{Ir-O}}(\text{Å})$	$\theta_{\text{Ir-O-Ir}}(^{\circ})$
Mn	I	5.167	2.986	1.997	95.92
	II	5.127	2.962	2.009	95.57
	III	5.152	2.977	1.985	95.96
Fe	I	5.104	2.951	2.012	94.32
	II	5.068	2.930	2.004	94.00
	III	5.083	2.940	2.008	93.98
Co	I	5.116	2.961	1.999	94.76
	II	5.113	2.955	1.990	95.26
	III	5.115	2.960	2.019	94.31
Ni	I	5.148	2.977	2.006	95.03
	II	5.181	2.994	1.997	96.69
	III	5.173	2.994	1.995	94.18
bulk [56]		5.158	2.986	1.942	94.03

III. METHODS

A. *Ab initio* calculations

In the *ab initio* calculations, we use the QUANTUM ESPRESSO [60] based on the density functional theory [61]. The exchange-correlation potential is treated as Perdew-Zunger functional by using the projector-augmented-wave method [62, 63]. Under the consideration of the SOC effect, the fully relativistic functional is utilized for all the atoms except oxygens [64]. To obtain stable structures for heterostructures, we initially construct a bilayer MgIrO_3 structure using the experimental structure for the bulk material. Subsequently, we replace the lower half with ATiO_3 layer to create three different types of heterostructures in Fig. 1. Then, we perform full optimization for both lattice parameters and the position of each ion until the residual force becomes less

than 0.0001 Ry/Bohr. During the optimization procedure, the structural symmetry is retained as $R\bar{3}$ space group. The 20 Å thick vacuum is adopted to eliminate the interaction between adjacent layers. The $6 \times 6 \times 1$ and $12 \times 12 \times 1$ Monkhorst-Pack k -points meshes are utilized for the structural optimization and self-consistent calculations, respectively [65]. The self-consistent convergence is set to 10^{-8} Ry and the kinetic energy is chosen to 80 Ry for all the structural configurations, which are respectively small and large enough to guarantee accurate results. To simulate the electron correlation effects for $3d$ electrons of A atoms and $5d$ electrons of Ir atom, we adopt the LDA+SOC+ U calculations [66] with the Coulomb repulsions $U_A = 5.0$ eV, 5.3 eV, 4.5 eV, and 6.45 eV with $A = \text{Mn, Fe, Co, and Ni}$ atoms, respectively, and $U_{\text{Ir}} = 3.0$ eV, accompanying with the Hund's-rule coupling with $J_H/U = 0.1$ according to previous works [67, 68].

Based on the *ab initio* results, we also obtain the MLWFs by using the k points increased to $18 \times 18 \times 1$ within the Monkhorst-Pack scheme [65]. We select the t_{2g} , $2p$, and $3d$ orbitals respectively of Ir, O, and A atoms to construct the MLWFs by employing the Wannier90 [69]. Herein, we include O $2p$ and A $3d$ orbitals due to their significant contribution near the Fermi level, as detailed in Figs. 2-5. By utilizing the MLWFs, we construct the tight-binding models and calculate their band structures for comparison. We also calculate the PDOS of each atomic orbital, including the effective angular momentum of Ir atoms j_{eff} , from the tight-binding models. We consider the non-relativistic *ab initio* calculations and relative MLWFs for the estimation of transfer integrals (see Sec. III B).

B. Multiorbital Hubbard model

To estimate the effective exchange interactions between the magnetic Ir ions, we need the effective transfer integrals between neighboring Ir t_{2g} orbitals with the association of O $2p$ orbitals by constructing MLWFs with LDA calculation in the paramagnetic state. It is noticeable that the effects of relativistic SOC and electron correlation are not taken into account in this calculation to circumvent the doublecounting in constructing the effective spin models. Specifically, the effective transfer integral t is estimated as [57]

$$t_{iu,jv} + \sum_p \frac{t_{iu,p} t_{jv,p}^*}{\Delta_{p-uv}}. \quad (2)$$

The first term denotes the direct hopping between two adjacent Ir atoms, where $t_{iu,jv}$ represents the transfer integral between orbital u at site i and orbital v at site j . The second term denotes the indirect hopping between the two Ir atoms via the shared O $2p$ orbitals, where $t_{iu,p}$ represents the transfer integral between Ir atom u orbital at site i and ligand atom p orbital, and Δ_{p-uv}

is the harmonic mean of the energy of u and v orbitals measured from that of p orbitals. Herein, we consider only hopping processes between the nearest-neighbor Ir atoms.

Using the effective transfer integrals, we construct a multiorbital Hubbard model with one hole occupying the t_{2g} orbitals, whose Hamiltonian is given by

$$H = H_{\text{hop}} + H_{\text{tri}} + H_{\text{soc}} + H_U. \quad (3)$$

The first term denotes the kinetic energy of the t_{2g} electrons as

$$H_{\text{hop}} = - \sum_{i,j} \mathbf{c}_i^\dagger (\hat{T}_{ij}^\gamma \otimes \sigma_0) \mathbf{c}_j, \quad (4)$$

where the matrix \hat{T}_{ij}^γ includes the effective transfer integrals estimated by Eq. (2), γ is the x , y , and z bond connected by neighboring sites i and j which belong to different honeycomb sublattices, and σ_0 denotes the 2×2 identity matrix; $\mathbf{c}_i^\dagger = (c_{i,yz,\uparrow}^\dagger, c_{i,yz,\downarrow}^\dagger, c_{i,zx,\uparrow}^\dagger, c_{i,zx,\downarrow}^\dagger, c_{i,xy,\uparrow}^\dagger, c_{i,xy,\downarrow}^\dagger)$ denote the creation of one hole in the t_{2g} orbitals (yz , zx , and xy) carrying spin up (\uparrow) or down (\downarrow) at site i . The second term in Eq. (3) denotes the trigonal crystal splitting as

$$H_{\text{tri}} = - \sum_i \mathbf{c}_i^\dagger (\hat{T}_{\text{tri}} \otimes \sigma_0) \mathbf{c}_i, \quad (5)$$

with \hat{T}_{tri} in the form of

$$\hat{T}_{\text{tri}} = \begin{pmatrix} 0 & \Delta_{\text{tri}} & \Delta_{\text{tri}} \\ \Delta_{\text{tri}} & 0 & \Delta_{\text{tri}} \\ \Delta_{\text{tri}} & \Delta_{\text{tri}} & 0 \end{pmatrix}. \quad (6)$$

The third term denotes the SOC as

$$H_{\text{soc}} = - \frac{\lambda}{2} \sum_i \mathbf{c}_i^\dagger \begin{pmatrix} 0 & i\sigma_z & -i\sigma_y \\ -i\sigma_z & 0 & i\sigma_x \\ i\sigma_y & -i\sigma_x & 0 \end{pmatrix} \mathbf{c}_i, \quad (7)$$

where $\sigma_{\{x,y,z\}}$ are Pauli matrices, and λ is the SOC coefficient; for instance, λ of Ir atom is estimated at about 0.4 eV [70, 71]. The last term denotes the onsite Coulomb interactions as [72, 73]

$$\begin{aligned} H_U = & \sum_i U n_{iu\uparrow} n_{iu\downarrow} \\ & + \sum_{i,u<v,\sigma} [U' n_{iu\sigma} n_{iv\bar{\sigma}} + (U' - J_H) n_{iu\sigma} n_{iv\sigma}] \\ & + \sum_{i,u \neq v} J_H (c_{iu\uparrow}^\dagger c_{iv\downarrow}^\dagger c_{iu\downarrow} c_{iv\uparrow} + c_{iu\uparrow}^\dagger c_{iu\downarrow}^\dagger c_{iv\downarrow} c_{iv\uparrow}) \end{aligned} \quad (8)$$

with $n_{iu\sigma} = c_{iu\sigma}^\dagger c_{iu\sigma}$; $\bar{\sigma} = \downarrow$ (\uparrow) for $\sigma = \uparrow$ (\downarrow). In Eq. (8), the first, second, and third summations represent the intraorbital Coulomb interaction in the same orbital with opposite spins, the interorbital Coulomb interactions between orbital u and orbital v , and the spin-flip and pair-hopping processes, respectively.

C. Second-order perturbation

For Ir⁵⁺ ions, the t_{2g} manifold splits into a doublet and a quartet under the SOC, which are respectively characterized by the pseudospin $j_{\text{eff}} = 1/2$ and $3/2$. In the ground state, the latter is fully occupied and the former is half filled, which is described by the Kramers doublet $|j_{\text{eff}} = 1/2, +\rangle$ and $|j_{\text{eff}} = 1/2, -\rangle$ [27, 74]:

$$|j_{\text{eff}} = 1/2, +\rangle = \frac{1}{\sqrt{3}} (|d_{yz} \downarrow\rangle + i|d_{zx} \downarrow\rangle + |d_{xy} \uparrow\rangle), \quad (9)$$

$$|j_{\text{eff}} = 1/2, -\rangle = \frac{1}{\sqrt{3}} (|d_{yz} \uparrow\rangle - i|d_{zx} \uparrow\rangle - |d_{xy} \downarrow\rangle). \quad (10)$$

When the system is in the spin-orbit coupled Mott insulating state with the low-spin d^5 configuration, the low-energy physics can be described by the pseudospin $j_{\text{eff}} = 1/2$ degree of freedom. In this case, the effective exchange interactions between the pseudospins can be estimated by using the second-order perturbation theory in the atomic limit, where the three terms in Eq. (3), $H_{\text{tri}} + H_{\text{soc}} + H_U$, are regarded as unperturbed Hamiltonian, and H_{hop} is treated as perturbation. The energy correction for a neighboring pseudospin pair in the second-order perturbation is given by

$$E_{\sigma'_i, \sigma'_j; \sigma_i, \sigma_j}^{(2)} = \sum_n \frac{\langle \sigma'_i \sigma'_j | H_{\text{hop}} | n \rangle \langle n | H_{\text{hop}} | \sigma_i \sigma_j \rangle}{E_0 - E_n}, \quad (11)$$

where σ_i and σ'_i denote the pseudospin $+$ or $-$ at site i , $|\sigma_i \sigma_j\rangle$ and $\langle \sigma'_i \sigma'_j |$ is the initial and final states during the perturbation process, respectively, and $|n\rangle$ is the intermediate state with $5d^4$ - $5d^6$ or $5d^6$ - $5d^4$ electron configuration; E_0 is the ground state energy for the $5d^5$ - $5d^5$ electron configuration, and E_n is the energy eigenvalue for the intermediate state $|n\rangle$. Here, $|n\rangle$ and E_n are obtained by diagonalizing the unperturbed Hamiltonian $H_{\text{tri}} + H_{\text{soc}} + H_U$.

The effective pseudospin Hamiltonian is written in the form of

$$H = \sum_{\gamma=x,y,z} \sum_{\langle i,j \rangle} \mathbf{S}_i^\text{T} \mathbf{J}_{ij}^\gamma \mathbf{S}_j, \quad (12)$$

where i, j denote the neighboring sites, and γ denotes the three types of Ir-Ir bonds on the MgIrO₆ honeycomb layer that are related by C_3 rotation. The coupling constant \mathbf{J}_{ij}^γ is explicitly given, e.g., for the z bond as

$$\mathbf{J}_{ij}^z = \begin{bmatrix} J & \Gamma & \Gamma' \\ \Gamma & J & \Gamma' \\ \Gamma' & \Gamma' & K \end{bmatrix}, \quad (13)$$

where J , K , Γ , and Γ' represent the coupling constants for the isotropic Heisenberg interaction, the bond-dependent Ising-like Kitaev interaction, and two types of the symmetric off-diagonal interactions. Using the perturbation energy $E_{\sigma'_i, \sigma'_j; \sigma_i, \sigma_j}^{(2)}$ obtained by Eq. (11), the

coupling constants are calculated as

$$J = 2E_{+,-;-,+}^{(2)}, \quad (14)$$

$$K = 2 \left(E_{+,+;+,+}^{(2)} - E_{+,-;+,-}^{(2)} \right), \quad (15)$$

$$\Gamma = 2\text{Im} \left\{ E_{-,-;+,+}^{(2)} \right\}, \quad (16)$$

$$\Gamma' = 4\text{Re} \left\{ E_{+,+;+,-}^{(2)} \right\}. \quad (17)$$

IV. ELECTRONIC BAND STRUCTURE

A. LDA+SOC results for paramagnetic states

Let us begin with the electronic band structures from LDA+SOC calculations. The results for MgIrO₃/ATiO₃ with $A = \text{Mn, Fe, Co, and Ni}$ are shown in Figs. 2(a), 3(a), 4(a), and 5(a), respectively. Here we display the band structures in the paramagnetic state obtained by the *ab initio* calculations (black solid lines) and the MLWF analysis (blue dashed lines), together with the atomic orbitals PDOS including $5d$ of Ir atoms, $3d$ of A atoms, and $2p$ of O atoms related to IrO₆ and AO₆ octahedra. It is obvious that the systems are metallic for all the types of heterostructures, regardless of the choice of A atoms. The strong SOC splits the t_{2g} bands of Ir atoms into $j_{\text{eff}} = 1/2$ and $j_{\text{eff}} = 3/2$ bands, as depicted in the PDOS. Specifically, the $j_{\text{eff}} = 1/2$ bands are predominated to form the metallic bands in the proximity of the Fermi level, covering the energy region almost from -1.0 eV to 0.2 (0.4) eV for $A = \text{Mn}$ with type-II (type-I and III), from -0.8 eV to 0.2 eV for $A = \text{Fe}$ with all types, from -0.6 (-1.0) eV to 0.2 eV for $A = \text{Co}$ with type-II (type-I and III), and from -0.4 eV to 0.4 eV for $A = \text{Ni}$ with type-I and II, and -0.8 eV to 0.2 eV with type-III. On the other hand, the $j_{\text{eff}} = 3/2$ bands primarily occupy the energy region below the $j_{\text{eff}} = 1/2$ bands.

From the PDOS in right panels of Figs. 2(a), 3(a), 4(a), and 5(a), the $3d$ bands of A atoms and the O $2p$ bands of AO₆ octahedra simultaneously across the Fermi level, with hybridization with the Ir $5d$ bands. Notably, the energy range of the A $3d$ bands closely overlaps with that of the Ir $5d$ $j_{\text{eff}} = 1/2$ bands for $A = \text{Mn and Fe}$, but it overlaps with both $j_{\text{eff}} = 1/2$ and $j_{\text{eff}} = 3/2$ manifold for $A = \text{Co and Ni}$. As to the O $2p$ bands, the energy range of the PDOS overlaps with that for corresponding Ir $5d$ or A $3d$ encapsulated in the octahedra, suggesting Ir-O and A-O hybridization.

B. LDA+SOC+ U results for magnetic states

1. Magnetic ground states

The bulk counterpart of each constituent of the heterostructures exhibits some magnetic long-range orders

in the ground state. In the bulk MgIrO₃, Ir ions show a zigzag-type AFM order with the magnetic moments lying almost within the honeycomb plane [58]. In the bulk ATiO₃, the $A = \text{Mn and Fe}$ ions show Néel-type AFM orders with out-of-plane magnetic moments [75], while the $A = \text{Co and Ni}$ ions support Néel orders with in-plane magnetic moments [75, 76]. It is intriguing to examine how these magnetic orders in the bulk are affected by making heterostructures. We determine the stable magnetic ground states for each heterostructure through *ab initio* calculations by including the effect of electron correlations based on the LDA+SOC+ U method. To determine the potential magnetic ground state for each heterostructure, we compare the energy across a total of 16 magnetic configurations among all combinations of following types of the magnetic orders: FM and Néel orders with in-plane and out-of-plane magnetic moments for A layer, and Néel and zigzag orders with in-plane magnetic moments, as well as FM with in-plane and out-of-plane magnetic moments for Ir layer, within a $2 \times 2 \times 1$ supercell setup.

TABLE II. Stable magnetic orders obtained by the LDA+SOC+ U calculations: FM, Néel, and zigzag denotes the ferromagnetic, Néel-type antiferromagnetic, and zigzag-type antiferromagnetic orders, respectively. While the directions of the magnetic moments are all in-plane for the Ir layers, those for A can be in-plane (“in”) or out-of-plane (“out”) depending on A and type of the heterostructure.

A	layer	type-I	II	III
Mn	Ir	in-zigzag	in-zigzag	in-zigzag
	Mn	in-Néel	out-FM	in-Néel
Fe	Ir	in-Néel	in-Néel	in-FM
	Fe	out-Néel	in-FM	in-FM
Co	Ir	out-FM	in-FM	in-Néel
	Co	in-Néel	in-Néel	in-Néel
Ni	Ir	in-Néel	in-zigzag	in-zigzag
	Ni	out-Néel	in-FM	in-Néel

The results of the most stable magnetic state are listed in Table II. The details of the energy comparison are shown in Appendix A. In most cases, the A ions show Néel orders as in the bulk cases, but the direction of magnetic moments is changed from the bulk in some cases. For instance, type-I and III with $A = \text{Mn}$ and type-III with $A = \text{Fe}$ switch the moment direction from out-of-plane to in-plane. While all the types with $A = \text{Co}$ retain the in-plane Néel states, type-I with $A = \text{Ni}$ is changed into the out-of-plane Néel state. The results indicate that the direction of magnetic moments are sensitively altered by making the heterostructures with MgIrO₃. Meanwhile, the other cases, type-II with $A = \text{Mn, Fe, and Ni}$ as well as type-III with $A = \text{Fe}$, are stabilized in the FM state. These results are in good accordance with the effective magnetic couplings between the A ions estimated by a similar perturbation theory in Sec. III C [77, 78], attesting to the reliability of magnetic properties in heterostructures (see Appendix A).

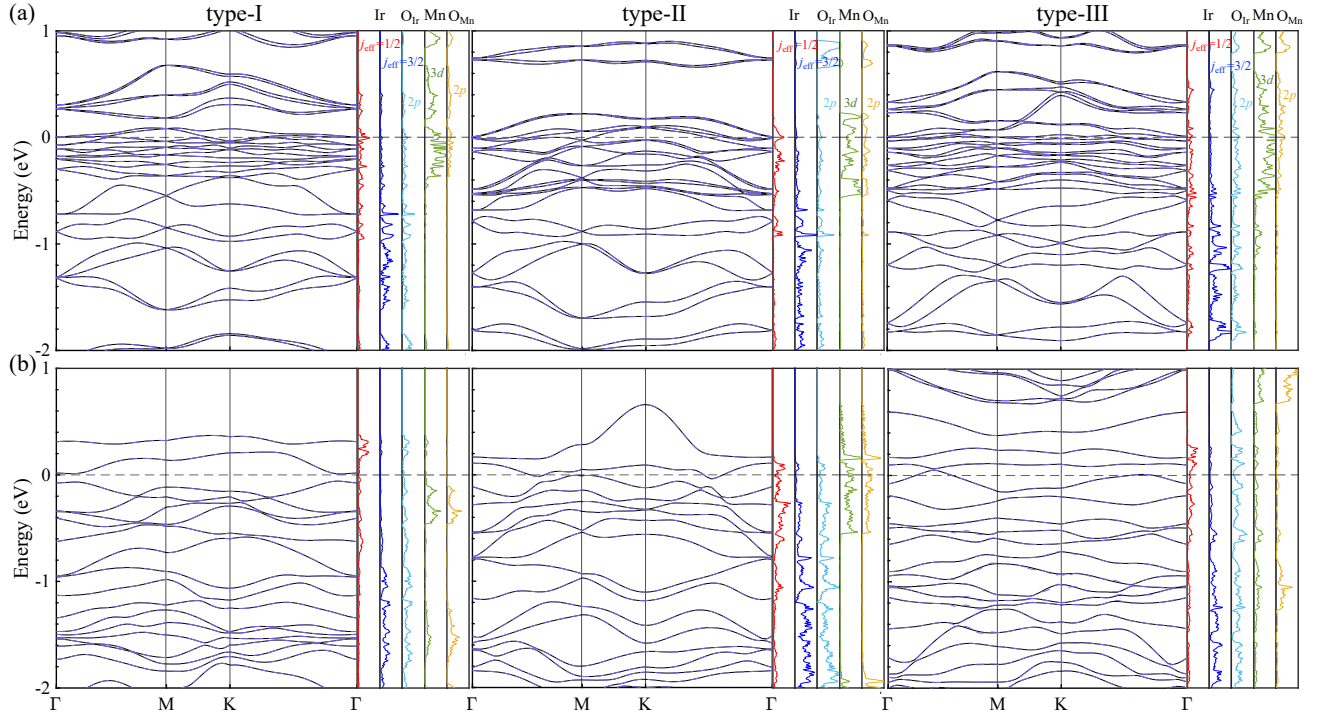


FIG. 2. The band structures of $\text{MgIrO}_3/\text{MnTiO}_3$ for type-I, II, and III with (a) the LDA+SOC calculations for the paramagnetic state and (b) the LDA+SOC+ U calculations for the stable magnetic orders (see Sec. IV B 2). The black lines represent the electronic structure obtained by the *ab initio* calculations, and the light-blue dashed curves represent the electronic dispersions obtained by tight-binding parameters using the MLWFs. The right panels in each figure denote the PDOS for different orbitals on specific atoms: The red and blue lines represent the j_{eff} manifolds of Ir atoms, the cyan and orange lines represent the $2p$ orbitals of O atoms in IrO_6 octahedra (O_{Ir}) and MnO_6 octahedra (O_{Mn}), respectively, and the green line represents the $3d$ orbitals of Mn atoms. The Fermi energy is set to zero.

The magnetic states in the Ir layer are more complex due to the possibility of the zigzag state. For $A = \text{Mn}$, the magnetic ground states of the Ir layer in all three types prefer the in-plane zigzag state as in the bulk of MgIrO_3 . In contrast, for $A = \text{Fe}$, type-I and II are stable in the in-plane Néel state, but type-III prefers the in-plane FM state. For $A = \text{Co}$, only type-III stabilizes the in-plane Néel state, while others exhibit the out-of-plane FM state for type-I and the in-plane FM state for type-II. Lastly, for $A = \text{Ni}$, both type-II and type-III prefer the in-plane zigzag state, while it changes into the in-plane Néel state in type-I. These results indicate that the magnetic state in the Ir honeycomb layer is susceptible to both A ions and the heterostructure type. We will discuss this point from the viewpoint of the effective magnetic couplings in Sec. V.

2. Band structures

We present the band structures obtained by the LDA+SOC+ U calculations in Figs. 2(b), 3(b), 4(b), and 5(b) for $A = \text{Mn}$, Fe, Co, and Ni, respectively. In these calculations, we adopt the stable magnetic states in Table II, except for the cases with in-plane zigzag order in

the Ir layer. For the zigzag cases, for simplicity, we replace them by the in-plane Néel solutions, keeping the A layer the same as the stable one. This reduces significantly the computational cost of the MLWF analysis for the zigzag state with a larger supercell. We confirm that the band structures for the Néel state are similar to those for the zigzag state, and the energy differences between the two states are not large as shown in Appendix A.

When we turn on Coulomb repulsions for both Ir and A atoms, most of the type-I and III heterostructures become insulating, except for Mn type-III. The band gaps, obtained by $E_g = E_c - E_v$, are shown in Fig. 6, where E_c denotes the energy of conduction band minimum and E_v is that of valence band maximum. In all cases, except for type-I with $A = \text{Mn}$ and Ni and type-III with $A = \text{Co}$, the gap is defined by the $j_{\text{eff}} = 1/2$ bands of Ir ions, that is, both conduction and valence bands are $j_{\text{eff}} = 1/2$, and the $j_{\text{eff}} = 1/2$ bands is half filled. It is worth highlighting that there are four $j_{\text{eff}} = 1/2$ bands, which originate from different sites of Ir atoms with opposite magnetic moments; in the bulk and monolayer cases they are degenerate in pair [57], but the degeneracy is lifted in the heterostructures and two out of four are occupied in the half-filled insulating state. Meanwhile, in the cases of type-I with $A = \text{Mn}$ and Ni and type-III with $A = \text{Co}$,

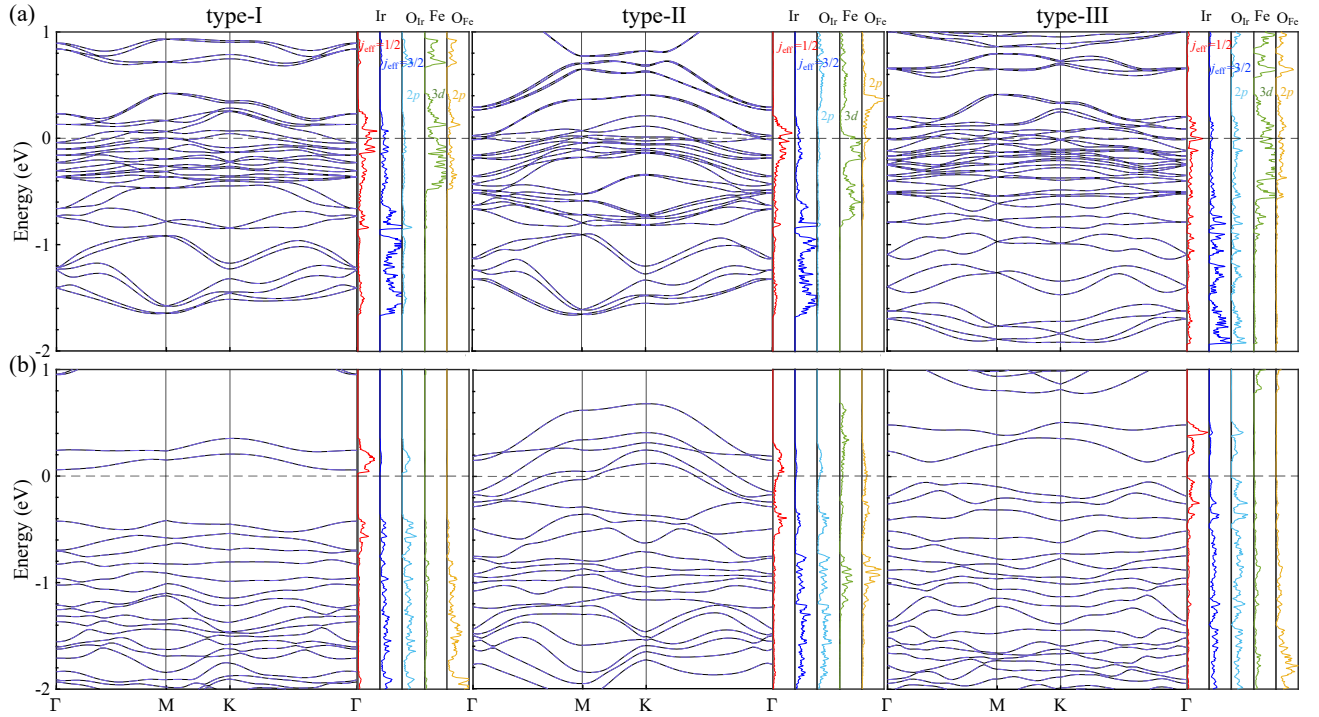


FIG. 3. The band structures of $\text{MgIrO}_3/\text{FeTiO}_3$ for type-I, II, and III obtained by (a) the LDA+SOC calculations for the paramagnetic state and (b) the LDA+SOC+ U calculations for the stable magnetic orders (see Sec. IV B 2). The notations are common to Fig. 2.

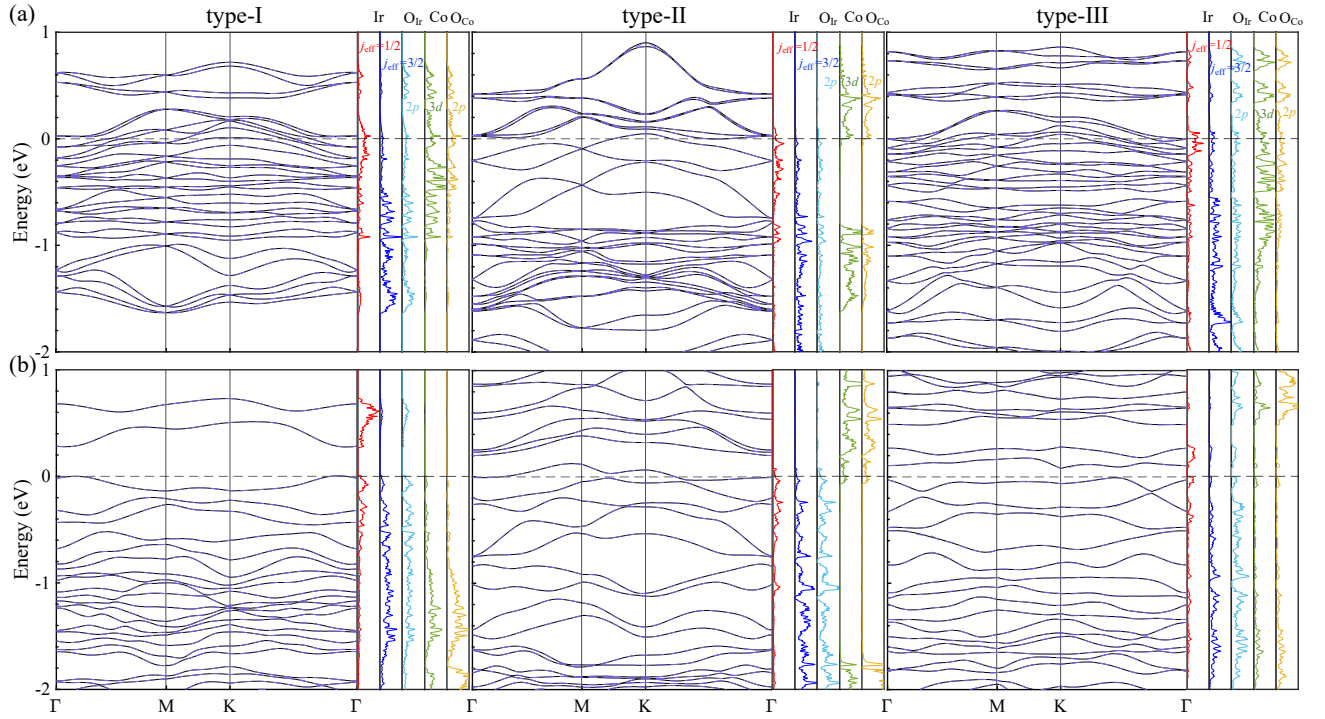


FIG. 4. The band structures of $\text{MgIrO}_3/\text{CoTiO}_3$ for type-I, II, and III obtained by (a) the LDA+SOC calculations for the paramagnetic state and (b) the LDA+SOC+ U calculations for the stable magnetic orders (see Sec. IV B 2). The notations are common to Fig. 2.

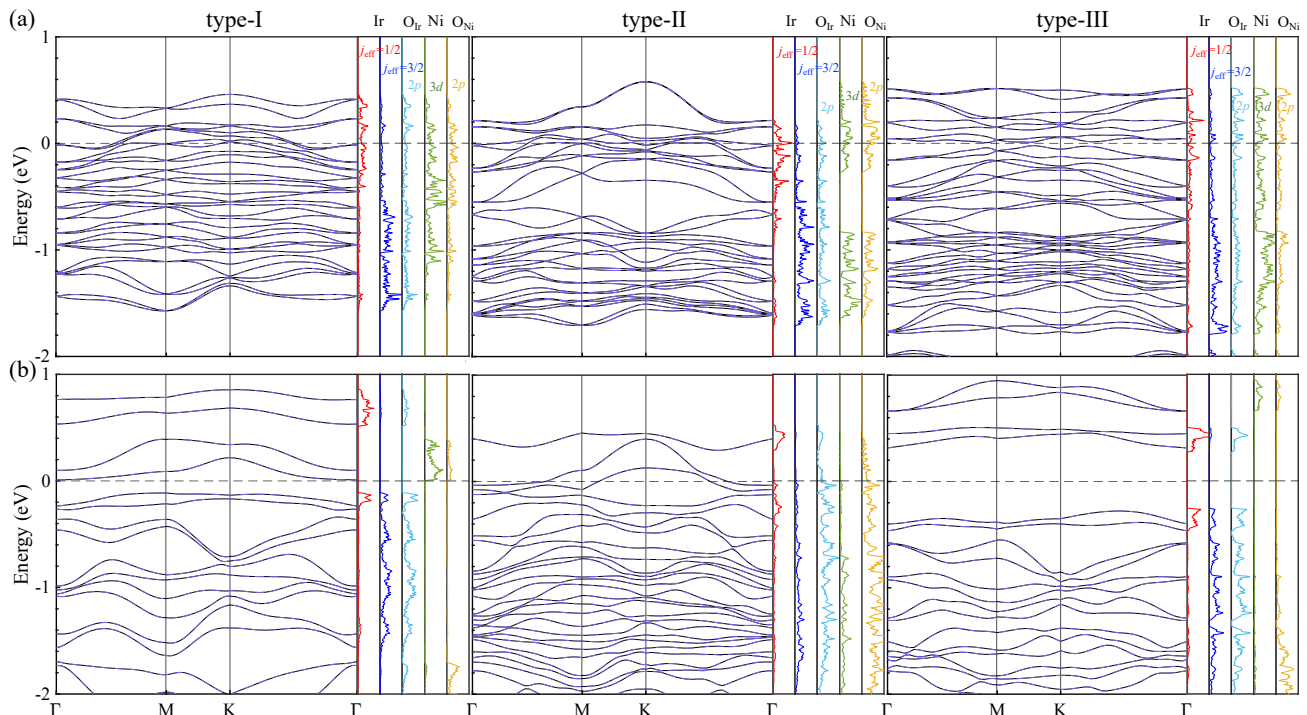


FIG. 5. The band structures of $\text{MgIrO}_3/\text{NiTiO}_3$ for type-I, II, and III obtained by (a) the LDA+SOC calculations for the paramagnetic state and (b) the LDA+SOC+ U calculations for the stable magnetic orders (see Sec. IV B 2). The notations are common to Fig. 2.

the $3d$ bands of A ions hybridized with O $2p$ orbitals intervene near the Fermi level, and the gap is defined between the $j_{\text{eff}} = 1/2$ and $3d$ bands. In these cases, however, a larger gap is well preserved in the $j_{\text{eff}} = 1/2$ bands, as shown in Figs. 2(b), 4(b), and 5(b). We note that the Co type-III is a further exception since the gap opens between the highest-energy $j_{\text{eff}} = 1/2$ band and the Co $3d$ band; the $j_{\text{eff}} = 1/2$ bands are not half filled but $3/4$ filled (see Appendix B). We plot the band gap defined by the $j_{\text{eff}} = 1/2$ bands by red asterisks in Fig. 6, including the $3/4$ -filled case for the Co type-III.

These results clearly indicate that the inclusion of both SOC and U effects results in the opening of a band gap in the $j_{\text{eff}} = 1/2$ bands at half filling in type-I and III heterostructures excluding Mn type-III and Co type-III. This suggests the formation of spin-orbit coupled Mott insulators in the Ir honeycomb layers, which are cornerstone of the Kitaev candidate materials [27], motivating us to further investigate the effective exchange interaction in Sec. V. The Co type-III is in an interesting state with $3/4$ filling of $j_{\text{eff}} = 1/2$ bands, but we exclude it from the following analysis of the effective exchange interactions in Sec. V.

Distinct from the emergence of spin-orbit coupled Mott insulator, the LDA+SOC+ U band structures show metallic states for type-II heterostructures. The $j_{\text{eff}} = 1/2$ bands do not show a clear gap and cross the Fermi level, resulting in the spin-orbit coupled metals. Notably, in all cases, the upper $j_{\text{eff}} = 1/2$ bands are partially

TABLE III. Electronic states of each heterostructure obtained by the LDA+SOC+ U calculations. SOCI and SOCM denote spin-orbit coupled insulator and metal, respectively. e and h in the parentheses represent the carriers in the SOCM doped to the mother SOCI. The asterisk for the Co type-III indicates that the system is in the $3/4$ -filled insulating state of the $j_{\text{eff}} = 1/2$ bands.

A	type-I	II	III
Mn	SOCI	SOCM(e)	SOCM(h)
Fe	SOCI	SOCM(e)	SOCI
Co	SOCI	SOCM(e)	SOCI*
Ni	SOCI	SOCM(e)	SOCI

doped, realizing electron-doped Mott insulators. The doping rate varies with A atoms. We note that the type-III heterostructure of Mn also exhibits a metallic state, but in this case, holes are doped to the lower $j_{\text{eff}} = 1/2$ band. See Appendix B for the orbital projected band structures.

We summarize the electronic states in Table III. The type-I and III heterostructures are all spin-orbit coupled Mott insulators (SOCI) except for the type-III Mn case, while the type-II are all spin-orbit coupled metals (SOCM). For the SOCM, we also indicate the nature of carriers, electrons or holes; the type-II heterostructures are all electron doped, while the type-III Mn is hole doped.

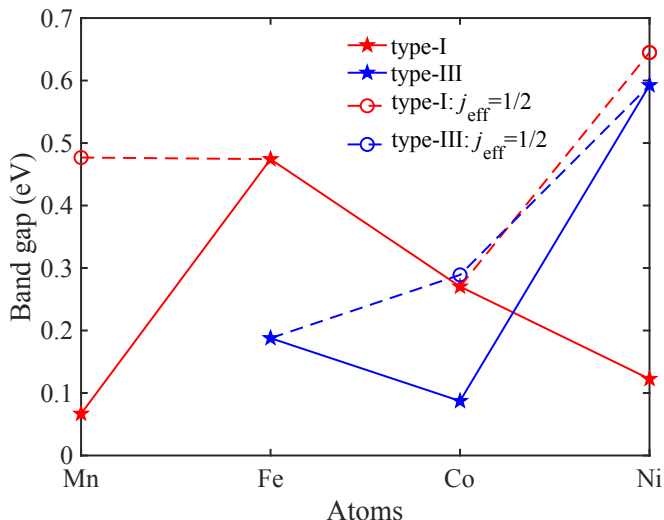


FIG. 6. The band gap in the insulating states for type-I and III obtained by the LDA+SOC+ U calculations. The open circles represent the gaps opening in the $j_{\text{eff}} = 1/2$ bands for Mn and Ni of type-I and Co of type-III. Note that the Co type-III is exceptional since the $j_{\text{eff}} = 1/2$ bands are at $3/4$ filling, rather than half filling in the other cases; see the text for details.

V. EXCHANGE INTERACTIONS

The electronic band structure analysis reveals the emergence of the spin-orbit coupled Mott insulating state in the MgIrO_6 layer of type-I and III heterostructures, except for the Mn and Co type-III. In these cases, the low-energy physics is expected to be described by effective pseudospin models with dominant Kitaev-type interactions [27]. The effective exchange interactions can be derived by means of the second-order perturbation for the multiorbital Hubbard model (Secs. IIIB and IIIC). We set $U_{\text{Ir}} = 3.0$ eV, $J_{\text{H}}/U_{\text{Ir}} = 0.1$, and $\lambda = 0.4$ eV in the perturbation calculations. The results are summarized in Fig. 7. For comparison, we also plot the estimates for monolayer and bulk MgIrO_3 . For the bulk case, its potential for hosting Kitaev spin liquids was demonstrated in the previous study [57]. Regarding the monolayer, we obtain the results from the band structures shown in Appendix C, which illustrate the preservation of the $j_{\text{eff}} = 1/2$ manifold and spin-orbit coupled insulating nature.

In type-I heterostructures, the dominant interaction is the FM Kitaev interaction $K < 0$ for almost all A atoms, except for Mn. Particularly for $A = \text{Ni}$, the absolute value of K is significantly larger than the others, even considerable when compared with the monolayer and bulk MgIrO_3 . The subdominant interaction is the off-diagonal symmetric interaction $\Gamma > 0$. The other off-diagonal symmetric interaction Γ' as well as the Heisenberg interaction J is weaker than them. In the Mn case, all the interactions are exceptionally weak, presumably because of the intervening Mn $3d$ band and its hybridiza-

tion with the Ir $j_{\text{eff}} = 1/2$ bands. Meanwhile, for the type-III heterostructures, since the Mn and Co cases exhibit a metallic state and $3/4$ occupation of $j_{\text{eff}} = 1/2$ bands, respectively, we only calculate the effective magnetic constants for Fe and Ni. In these cases also, the dominant interaction is the FM K , accompanied by the subdominant Γ interaction, as shown in Fig. 7(a).

Thus, in all cases except the Mn type-I heterostructure, the dominant magnetic interaction in the spin-orbit coupled Mott insulating state in the Ir honeycomb layer is effectively described by the FM Kitaev interaction. Since Γ' is smaller than the other exchange constants, the low-energy magnetic properties can be well described by the generic K - J - Γ model [79, 80], which has been widely and successfully applied to study the Kitaev QSLs. We summarize the obtained effective exchange interactions of K , J , and Γ by using the parametrization

$$(K, J, \Gamma) = \mathcal{N}(\sin\theta\sin\phi, \sin\theta\cos\phi, \cos\theta), \quad (18)$$

where $\mathcal{N} = (K^2 + J^2 + \Gamma^2)^{-1/2}$ is the normalization factor. Figure 7(b) presents the results except for Mn type-I. Our heterostructures distribute in the region near the FM K only case ($\theta = \pi/2$ and $\phi = 3\pi/2$). We find a general trend that larger A atoms make the systems closer to the FM K only case; the best is found for Ni type-I and III. In the previous studies for the K - J - Γ model [79, 80], a keen competition between different magnetic phases was found in this region, which does not allow one to conclude the stable ground state in the thermodynamic limit. Given that this region appears to be connected to the solvable point for the FM Kitaev QSL, our heterostructures provide a promising platform for investigating the Kitaev QSL physics and related phase competition by finely tuning the magnetic interactions via the proximity effect in the heterostructures.

VI. DISCUSSION

Our systematic study of ilmenite heterostructures $\text{MgIrO}_3/\text{ATiO}_3$ with $A = \text{Mn, Fe, Co, and Ni}$ reveals their fascinating electronic and magnetic properties. The heterostructures in the paramagnetic state are metallic in terms of band structures obtained by LDA+SOC, regardless of types and A atoms. When incorporating the effect of electron correlation by the LDA+SOC+ U calculations, type-II heterostructures remain metallic across entire A atoms, whereas type-I and III heterostructures turn into insulating states, except for Mn type-III. As a consequence, the electronic states of heterostructures are classified into the spin-orbit coupled insulators and metals, each holding unique properties. The insulating cases possess the $j_{\text{eff}} = 1/2$ pseudospin degree of freedom, and furnish a fertile playground to investigate the Kitaev QSL. In these cases, however, due to the magnetic proximity effects from the A layer, we may expect interesting modification of the QSL state, as discussed in Sec. VIA below. Meanwhile, the metallic cases open avenues for

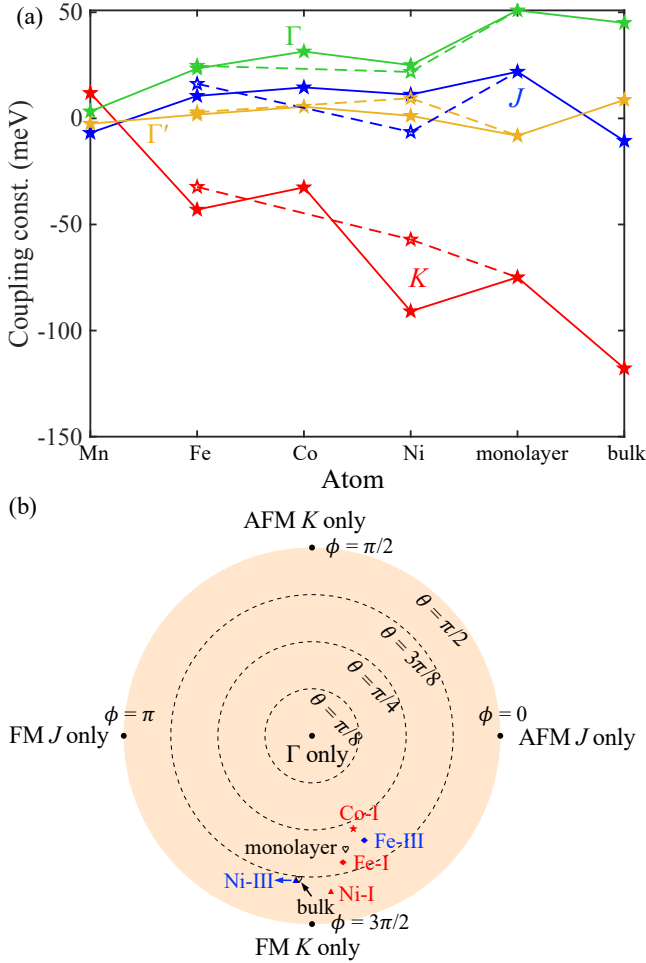


FIG. 7. The effective magnetic constants of heterostructures for different A atoms ($A = \text{Mn, Fe, Co, and Ni}$) of (a) type-I (solid line with pentagram) and type-III (dashed line with hollow pentagram). In (b), we summarize the results of K , J , and Γ in (a) except for Mn type-I by using the parametrization in Eq. (18). The parameters of the intraorbital Coulomb interaction, Hund's coupling, and spin-orbit coupling are set to $U_{\text{Ir}} = 3.0$ eV, $J_{\text{H}}/U_{\text{Ir}} = 0.1$, and $\lambda = 0.4$ eV, respectively, in the perturbation calculations.

exploring spin-orbit coupled metals, relatively scarce in strongly correlated systems [81–85]. In Sec. VIB, we discuss the possibility of exotic superconductivity in our self-doped heterostructures. In addition, we discuss the feasibility of fabrication of these heterostructures and identification of the Kitaev QSL nature in experiments in Sec. VIC.

A. Majorana Fermi surface by magnetic proximity effect

In the pure Kitaev model, the spins are fractionalized into itinerant Majorana fermions and localized Z_2 gauge fluxes [25]. The former has gapless excitations at the

nodal points of the Dirac-like dispersions at the K and K' points on the Brillouin zone edges, while the latter is gapped with no dispersion. When an external magnetic field is applied, the Dirac-like nodes of Majorana fermions are gapped out, resulting in the emergence of quasiparticles obeying non-Abelian statistics [25]. Beyond the uniform magnetic field, the Majorana dispersions are further modulated by an electric field and a staggered magnetic field [86, 87]. For instance, with the existence of the staggered magnetic field, the Dirac-like nodes at the K and K' points are shifted in the opposite directions in energy to each other, leading to the formation of the Majorana Fermi surfaces. Moreover, the introduction of both uniform and staggered magnetic fields can lead to further distinct modulations of the Majorana Fermi surfaces around the K and K' points, which are manifested by nonreciprocal thermal transport carried by the Majorana fermions [87].

In our heterostructures of type-I and III, the A layer supports a Néel order in most cases (Table II). It can generate an internal staggered magnetic field applied to the Ir layer through the magnetic proximity effect. This mimics the situations discussed above, and hence, it may result in the Majorana Fermi surfaces in the possible Kitaev QSL in the Ir layer. The combination of the uniform and staggered magnetic fields could also be realized by applying an external magnetic field to these heterostructures. Thus, the ilmenite heterostructures in proximity to the Kitaev QSL in the Ir layer hold promise for the formation of Majorana Fermi surfaces and resultant exotic thermal transport phenomena, providing a unique platform for identifying the fractional excitations in the Kitaev QSL.

B. Exotic superconductivity by carrier doping

QSLs have long been discussed as mother states of exotic superconductivity [19, 88, 89]. There, the introduction of mobile carriers to insulating QSLs possibly induces superconductivity in which the Cooper pairs are mediated by strong spin entanglement in the QSLs. A representative example discussed for a long time is high- T_c cuprates; here, the d -wave superconductivity is induced by carrier doping to the undoped antiferromagnetic state that is close to a QSL of so-called resonating valence bond (RVB) type [89–91]. A similar exotic superconducting state was also discussed for an iridium oxide Sr_2IrO_4 with spin-orbital entangled $j_{\text{eff}} = 1/2$ bands [92, 93]. Carrier doped Kitaev QSLs have also garnered extensive attention due to its potential accessibility to unconventional superconductivity that may possess more intricate pairing from the unique QSL properties. It was reported that doping into the Kitaev model with additional Heisenberg interactions (K - J model) led to a spin-triplet topological superconducting state [94], where the pairing nature is contingent upon the doping concentration. Furthermore, the competition between K and

J also significantly impacts the superconducting state; for example, K prefers a p -wave superconducting state, whereas J tends to favor a d -wave one [95, 96]. Even topological superconductivity is observed in an extended K - J - Γ model [97].

In the present work, we found metallic states in the spin-orbital coupled $j_{\text{eff}} = 1/2$ bands in the Ir layer for all type-II heterostructures (electron doping) and the type-III Mn heterostructure (hole doping) (see Table III). Besides, in the type-III Co heterostructure, electron doping occurs in the Ir layer, resulting in the $3/4$ -filled insulating state in the $j_{\text{eff}} = 1/2$ bands. These appealing results suggest that our ilmenite heterostructures offer a platform for studying exotic metallic and superconducting (even topological) properties with great flexibility by various choices of materials combination, which have been scarcely realized in the bulk systems.

C. Experimental feasibility

The bulk compounds of ilmenite $ATiO_3$ with $A = \text{Mn, Fe, Co, and Ni}$ have been successfully synthesized and investigated for over half a century due to its fruitful magnetic and novel electronic properties [75, 76, 98–100]. Technically, the Fe case, however, is more challenging compared to the others, as its synthesis needs very high pressure and high temperature conditions [101, 102]. Besides, the iridium ilmenite MgIrO_3 has also been synthesized as a power sample, where a magnetic phase transition was observed at 31.8 K [56]. The experimental lattice parameters are 5.14 Å for $ATiO_3$ with $A = \text{Mn}$ [75, 103–105], 5.09 Å for $A = \text{Fe}$ [101, 106, 107], 5.06 Å for $A = \text{Co}$ [76, 108, 109], and 5.03 Å for $A = \text{Ni}$ [75, 107, 110, 111], respectively, as well as that is 5.16 Å for MgIrO_3 . The relatively small lattice mismatch between these materials also ensure the possibility of combining them to create heterostructure with different compounds. Indeed, we demonstrated this in Sec. II; see Table I. More excitingly, the IrO_6 honeycomb lattice has been successfully incorporated into the ilmenite MnTiO_3 with the formation of several Mn-Ir-O layers [54]. This development lightens the fabrication of a supercell between MgIrO_3 and $ATiO_3$.

The verification of Kitaev QSL poses a significant challenge even though the successful synthesis of aforementioned heterostructures. First of all, it is crucial to identify the spin-orbital entangled electronic states with the formation of the $j_{\text{eff}} = 1/2$ bands in these heterostructures, as they are essential for the Kitaev interactions between the pseudospins. Several detectable spectroscopic techniques are useful for this purpose, applicable to both bulk and heterostructures [11, 34, 35, 39, 42, 43, 46, 112, 113]. Even the Kitaev exchange interaction can be directly uncovered in experiment [36, 37]. However, the key challenge lies in probing the intrinsic properties of Kitaev QSL, such as fractional spin excitations. Thus far, despite cooperative studies between theories

and experiments on, for instance, dynamical spin structure factors [44, 114–119] and the thermal Hall effect and its half quantization [45, 120–122], have been developed to identify the fractional excitations in Kitaev QSL, directly applying them on the heterostructures is still a great challenge. A promising experimental tool would be the Raman spectroscopy, given its successful application to not only bulk [41, 123, 124] but also atomically thin layers [125, 126]. The signals might be enhanced by piling up the heterostructures. Besides, many proposals for probing the Kitaev QSL in thin films and heterostructures have been recently made, such as local probes like scanning tunneling microscopy (STM) and atomic force microscopy (AFM) [127–131] as well as the spin Seebeck effect [132]. Additionally, as mentioned in Sec. VIA, the observation of the Majorana Fermi surfaces by thermal transport measurements in some particular heterostructures is also interesting.

VII. SUMMARY

To summarize, we have conducted a systematic investigation of the electronic and magnetic properties of the bilayer structures composed by the ilmenites $ATiO_3$ with $A = \text{Mn, Fe, Co, and Ni}$, in combination with the candidate for Kitaev magnets MgIrO_3 . We have designed and labeled three types of heterostructure, denoted as type-I, II, and III, distinguished by the atomic configurations at the interface. Our analysis of the electronic band structures based on the *ab initio* calculations has revealed that the spin-orbital coupled bands characterized by the pseudospin $j_{\text{eff}} = 1/2$, one of the fundamental component for the Kitaev interactions, is retained in the MgIrO_3 layer for all the types of heterostructures. We found that the $\text{MgIrO}_3/ATiO_3$ heterostructures of type-I and III are mostly spin-orbit coupled insulators, while those of type-II are spin-orbit coupled metals, irrespective of the A atoms. In the insulating heterostructures of type-I and III, based on the construction of the multiorbital Hubbard models and the second-order perturbation theory, we further found that the low-energy magnetic properties can be described by the $j_{\text{eff}} = 1/2$ pseudospin models in which the estimated exchange interactions are dominated by the Kitaev-type interaction. We showed that the parasitic subdominant interactions depend on the type of the heterostructure as well as the A atoms, offering the playground for systematic studies of the Kitaev spin liquid behaviors. Moreover, the stable Néel order in the $ATiO_3$ layer acts as a staggered magnetic field through the magnetic proximity effect, leading to the potential realization of Majorana Fermi surfaces in the MgIrO_3 layer. Meanwhile, in the metallic heterostructures of type-II as well as type-I Mn, we found that the nature of carriers and the doping rates vary depending on the heterostructures. This provides the possibility of systematically studying the spin-orbit coupled metals, including exploration of unconventional superconductivity

due to the unique spin-orbital entanglement.

In recent decades, significant progress has been made in the study of QSLs, primarily focusing on the discovery and expansion of new members in bulk materials. However, there has been limited exploration of creating and manipulating the QSLs in heterostructures despite the importance for device applications. Our study has demonstrated that the Kitaev-type QSL could be surveyed in ilmenite oxide heterostructures, displaying remarkable properties distinct from the bulk counterpart, such as flexible tuning of the Kitaev-type interactions and other parasitic interactions, and carrier doping to the Kitaev QSL. Besides the van der Waals heterostructures such as the combination of α -RuCl₃ and graphene, our finding would enlighten an additional route to explore the Kitaev QSL physics including the utilization of Majorana and anyonic excitations for future topological computing devices.

ACKNOWLEDGMENTS

We thank Y. Kato, M. Negishi, S. Okumura, A. Tsukazaki, and L. Zh. Zhang, for fruitful discussions. This work was supported by JST CREST Grant (No. JPMJCR18T2). Parts of the numerical calculations were performed in the supercomputing systems of the Institute for Solid State Physics, the University of Tokyo.

Appendix A: Detailed *ab initio* data for energy and magnetic coupling

In this Appendix, we present the details of *ab initio* results for various types of heterostructures. Tables IV-VII list the energy differences between different magnetic states for MgIrO₃/ATiO₃ heterostructures with $A = \text{Mn, Fe, Co, and Ni}$. The bold elements in these tables are the lowest-energy state in each type, utilized for the calculations of band structures in Sec. IV B 1. We also show in Table VIII the effective magnetic coupling constants between A atoms, in which negative and positive value indicates the FM and AFM coupling, respectively. Note that the A atoms comprise a triangular lattice at the interface in type I, a honeycomb lattice at the ATiO₃ layer, and a honeycomb lattice at the interface, as depicted in Fig. 1.

Appendix B: Orbital projected band structures

In this Appendix, we show the projection of the band structure to the Ir $5d$ orbitals for type-II heterostructures in Fig. 8 and type-III of Mn and Co in Fig. 9. The green shaded bands include high-energy four $j_{\text{eff}} = 1/2$ bands and low-energy eight $j_{\text{eff}} = 3/2$ bands. The results in Fig. 8 indicate that electrons are doped to the half-filled $j_{\text{eff}} = 1/2$ bands, realizing the spin-orbit coupled metallic

TABLE IV. Energy differences between different magnetic ordered states obtained by the LDA+SOC+ U calculations for MgIrO₃/MnTiO₃: FM, Néel, and zigzag denotes the ferromagnetic, Néel-type antiferromagnetic, and zigzag-type antiferromagnetic orders, respectively. While the directions of the magnetic moments are all in-plane for the Ir layers, those for A can be in-plane (“in”) or out-of-plane (“out”). The bold numbers denote the low-energy states used for calculating the band structures in Sec. IV B 1.

	magnetic state		energy/Ir (meV)		
	Ir	Mn	I	II	III
in-FM	in	FM	323.5	4.868	975.4
		Néel	1.492	46.52	1002
	out	FM	18.13	4.268	1065
		Néel	3.695	44.554	978.2
out-FM	in	FM	4.266	7.343	990.8
		Néel	0.773	43.68	993.2
	out	FM	35.71	1.584	1014
		Néel	76.55	40.34	879.6
Néel	in	FM	27.18	8.127	78.52
		Néel	26.98	42.83	48.51
	out	FM	20.45	4.474	121.0
		Néel	2.953	39.39	22.45
zigzag	in	FM	0.307	2.923	78.80
		Néel	0.000	21.55	0.000
	out	FM	20.05	0.000	120.49
		Néel	4.893	39.62	22.95

TABLE V. Energy differences between different magnetic ordered states for MgIrO₃/FeTiO₃. The notations are common to Table IV.

	magnetic state		energy/Ir (meV)		
	Ir	Fe	I	II	III
in-FM	in	FM	9.090	1.437	0.000
		Néel	17.00	15.75	13.14
	out	FM	15.71	21.80	2.631
		Néel	1.170	27.02	14.25
out-FM	in	FM	10.68	0.973	0.092
		Néel	12.12	0.948	13.01
	out	FM	55.58	21.13	1.739
		Néel	8.115	26.29	8.833
Néel	in	FM	24.64	0.000	0.056
		Néel	11.80	0.721	12.97
	out	FM	14.48	20.21	1.244
		Néel	0.000	25.37	8.596
zigzag	in	FM	15.58	1.233	0.056
		Néel	4.376	13.60	4.222
	out	FM	14.35	21.42	2.244
		Néel	4.743	26.59	9.608

states for all A atoms. The doping rates are large (small) for $A = \text{Mn and Co}$ (Fe and Ni). Meanwhile, Fig. 9(a) shows that the $j_{\text{eff}} = 1/2$ bands are slightly hole doped in the type-III with $A = \text{Mn}$. Figure 9(b) indicates that the type-III with $A = \text{Co}$ achieves an insulating state with $3/4$ -filled $j_{\text{eff}} = 1/2$ bands.

TABLE VI. Energy differences between different magnetic ordered states for $\text{MgIrO}_3/\text{CoTiO}_3$. The notations are common to Table IV.

magnetic state		energy/Ir (meV)			
Ir	Co	I	II	III	
in-FM	in	FM	188.2	20.02	0.795
		Néel	191.3	0.000	0.253
	out	FM	40.23	25.63	72.39
		Néel	1.201	235.7	87.28
out-FM	in	FM	0.174	20.06	0.800
		Néel	0.000	0.019	0.071
	out	FM	295.3	25.85	260.4
		Néel	47.55	0.044	49.64
Néel	in	FM	189.5	19.56	0.749
		Néel	184.3	19.36	0.000
	out	FM	17.53	24.82	33.16
		Néel	0.617	234.9	31.16
zigzag	in	FM	191.8	19.88	0.748
		Néel	189.6	19.39	1.969
	out	FM	40.81	25.45	34.02
		Néel	1.476	130.0	32.03

TABLE VII. Energy differences between different magnetic ordered states for $\text{MgIrO}_3/\text{NiTiO}_3$. The notations are common to Table IV.

magnetic state		energy/Ir (meV)			
Ir	Ni	I	II	III	
in-FM	in	FM	2.990	0.097	37.80
		Néel	4.998	70.93	35.99
	out	FM	3.536	1.255	26.76
		Néel	0.156	69.45	35.74
out-FM	in	FM	6.901	2.039	37.48
		Néel	7.311	70.74	35.98
	out	FM	20.94	2.385	24.79
		Néel	6.220	69.61	61.76
Néel	in	FM	14.06	1.678	48.98
		Néel	13.00	18.68	54.35
	out	FM	4.941	0.294	26.51
		Néel	0.000	18.631	37.36
zigzag	in	FM	4.971	0.000	36.97
		Néel	6.275	33.08	0.000
	out	FM	3.451	0.042	26.20
		Néel	3.876	68.36	35.45

Appendix C: Band structure of monolayer MgIrO_3

In this Appendix, we show the electronic band structures of monolayer MgIrO_3 obtained through *ab initio* calculations with the LDA+SOC [Fig. 10(a)] and LDA+SOC+ U scheme [Fig. 10(b)]. We set $U_{\text{Ir}} = 3.0$ eV and $J_{\text{H}}/U_{\text{Ir}} = 0.1$ in the LDA+SOC+ U calcu-

lations. In the LDA+SOC result, the system behaves as an insulating state with a tiny band gap of approximately ~ 0.096 eV. However, the introduction of U in the LDA+SOC+ U calculation results in a larger band gap, characteristic of the spin-orbit coupled insulator. We also calculate the PDOS of the $j_{\text{eff}} = 1/2$ and $3/2$

TABLE VIII. Effective magnetic coupling constants between the A atoms for three types of heterostructures. The unit is in meV.

A	type-I	II	III
Mn	0.667	-0.712	2.417
Fe	0.017	-0.607	-0.149
Co	0.065	0.262	6.458
Ni	0.088	-0.126	0.405

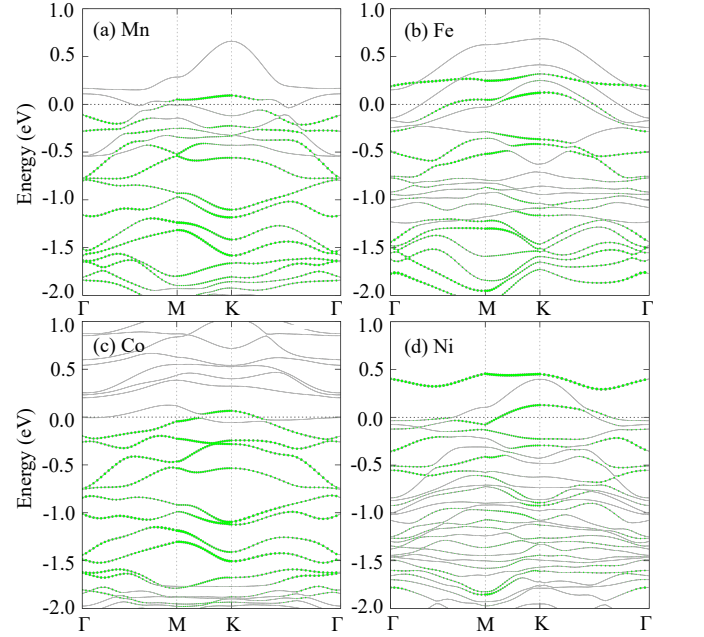


FIG. 8. Projection to the Ir $5d$ orbitals of the band structure for the type-II $\text{MgIrO}_3/\text{ATiO}_3$ heterostructures with (a) $A = \text{Mn}$, (b) Fe , (c) Co , and (d) Ni . The gray lines depict the band structures shown in the middle panels of Figs. 2(b)-5(b), and the green shade represents the weight of Ir $5d$ orbitals. The Fermi level is set to zero.

manifolds for Ir atoms, as shown in the right panels of Figs. 10(a) and 10(b). The PDOS of Ir atoms certifies that the $j_{\text{eff}} = 1/2$ and $j_{\text{eff}} = 3/2$ manifold are retained to support the spin-orbit coupled Mott insulating state in the monolayer, as in the bulk case [57].

[1] N. F. Mott, *Metal-Insulator Transition*, Rev. Mod. Phys. **40**, 677 (1968).

[2] M. Imada, A. Fujimori, and Y. Tokura, *Metal-Insulator Transitions*, Rev. Mod. Phys. **70**, 1039 (1998).

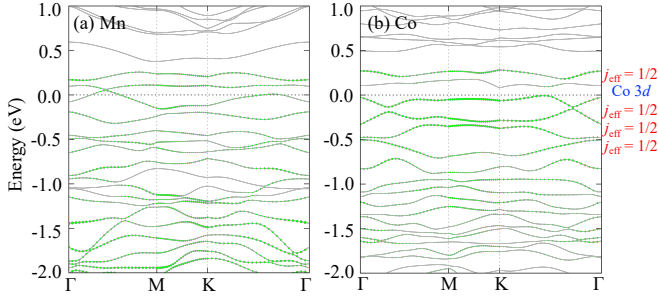


FIG. 9. Projection to the Ir 5d orbitals of the band structure for the type-III heterostructures of (a) MgIrO₃/MnTiO₃ and (b) MgIrO₃/CoTiO₃. The notations are common to Fig. 8.

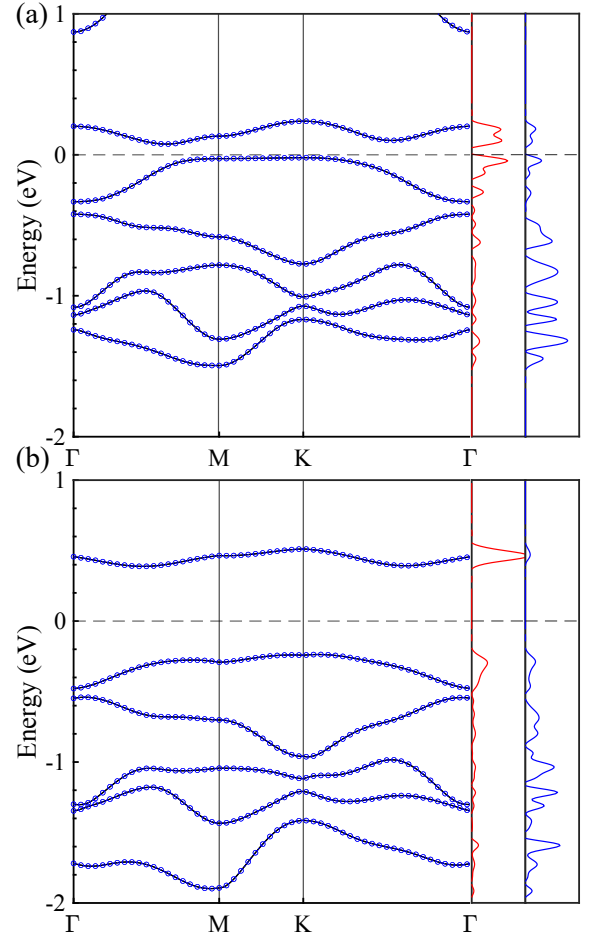


FIG. 10. Electronic band structure of monolayer MgIrO₃ obtained by the (a) LDA+SOC and (b) LDA+SOC+U calculations for the in-plane Néel AFM state. In (b), the parameters of the Coulomb interaction and Hund's coupling are respectively set to $U_{\text{Ir}} = 3.0$ eV and $J_{\text{H}}/U_{\text{Ir}} = 0.1$. The notions are common to Fig. 2.

- [3] X.-L. Qi and S.-C. Zhang, *Topological Insulators and Superconductors*, Rev. Mod. Phys. **83**, 1057 (2011).
- [4] M. Z. Hasan and C. L. Kane, *Colloquium: Topological insulators*, Rev. Mod. Phys. **82**, 3045 (2010).
- [5] X. Wan, A. Vishwanath, and S. Y. Savrasov, *Computational Design of Axion Insulators Based on 5d Spinel Compounds*, Phys. Rev. Lett. **108**, 146601 (2012).
- [6] D. M. Neno, C. A. Garcia, J. Gooth, C. Felser, and P. Narang, *Axion Physics in Condensed-Matter Systems*, Nat. Rev. Phys. **2**, 682 (2020).
- [7] X. Wan, A. M. Turner, A. Vishwanath, and S. Y. Savrasov, *Topological Semimetal and Fermi-Arc Surface States in the Electronic Structure of Pyrochlore Iridates*, Phys. Rev. B **83**, 205101 (2011).
- [8] A. A. Burkoff and L. Balents, *Weyl Semimetal in a Topological Insulator Multilayer*, Phys. Rev. Lett. **107**, 127205 (2011).
- [9] N. P. Armitage, E. J. Mele, and A. Vishwanath, *Weyl and Dirac Semimetals in Three-Dimensional Solids*, Rev. Mod. Phys. **90**, 015001 (2018).
- [10] W. Witczak-Krempa, G. Chen, Y. B. Kim, and L. Balents, *Correlated Quantum Phenomena in the Strong Spin-Orbit Regime*, Annu. Rev. Condens. Matter Phys. **5**, 57 (2014).
- [11] B. J. Kim, H. Jin, S. J. Moon, J.-Y. Kim, B.-G. Park, C. S. Leem, J. Yu, T. W. Noh, C. Kim, S.-J. Oh, J.-H. Park, V. Durairaj, G. Cao, and E. Rotenberg, *Novel $J_{\text{eff}} = 1/2$ Mott State Induced by Relativistic Spin-Orbit Coupling in Sr₂IrO₄*, Phys. Rev. Lett. **101**, 076402 (2008).
- [12] S. J. Moon, H. Jin, K. W. Kim, W. S. Choi, Y. S. Lee, J. Yu, G. Cao, A. Sumi, H. Funakubo, C. Bernhard, and T. W. Noh, *Dimensionality-Controlled Insulator-Metal Transition and Correlated Metallic State in 5d Transition Metal Oxides Sr_{n+1}Ir_nO_{3n+1} ($n = 1, 2$, and ∞)*, Phys. Rev. Lett. **101**, 226402 (2008).
- [13] M. K. Crawford, M. A. Subramanian, R. L. Harlow, J. A. Fernandez-Baca, Z. R. Wang, and D. C. Johnston, *Structural and Magnetic Studies of Sr₂IrO₄*, Phys. Rev. B **49**, 9198 (1994).
- [14] N. Read and B. Chakraborty, *Statistics of the Excitations of the Resonating-Valence-Bond State*, Phys. Rev. B **40**, 7133 (1989).
- [15] X.-G. Wen, *Topological Orders and Chern-Simons Theory in Strongly Correlated Quantum Liquid*, Int. J. Mod. Phys. B **5**, 1641 (1991).
- [16] P. W. Anderson, *Resonating Valence Bonds: A New Kind of Insulator?*, Mater. Res. Bull. **8**, 153 (1973).
- [17] L. Balents, *Spin Liquids in Frustrated Magnets*, Nature **464**, 199 (2010).
- [18] Y. Zhou, K. Kanoda, and T.-K. Ng, *Quantum Spin Liquid States*, Rev. Mod. Phys. **89**, 025003 (2017).
- [19] C. Broholm, R. Cava, S. Kivelson, D. Nocera, M. Norman, and T. Senthil, *Quantum Spin Liquids*, Science **367**, eaay0668 (2020).
- [20] C. Nayak, S. H. Simon, A. Stern, M. Freedman, and S. Das Sarma, *Non-Abelian Anyons and Topological Quantum Computation*, Rev. Mod. Phys. **80**, 1083 (2008).
- [21] P. W. Anderson, *Ordering and Antiferromagnetism in Ferrites*, Phys. Rev. **102**, 1008 (1956).
- [22] S. Sachdev, *Kagomé- and Triangular-Lattice Heisenberg Antiferromagnets: Ordering from Quantum Fluctuations and Quantum-Disordered Ground States with Unconfined Bosonic Spinons*, Phys. Rev. B **45**, 12377 (1992).

- [23] A. Ramirez, *Strongly Geometrically Frustrated Magnets*, Annu. Rev. Mater. Sci. **24**, 453 (1994).
- [24] Z. Nussinov and J. van den Brink, *Compass Models: Theory and Physical Motivations*, Rev. Mod. Phys. **87**, 1 (2015).
- [25] A. Kitaev, *Anyons in an Exactly Solved Model and Beyond*, Ann. Phys. **321**, 2 (2006).
- [26] A. Y. Kitaev, *Fault-Tolerant Quantum Computation by Anyons*, Ann. Phys. **303**, 2 (2003).
- [27] G. Jackeli and G. Khaliullin, *Mott Insulators in the Strong Spin-Orbit Coupling Limit: From Heisenberg to a Quantum Compass and Kitaev Models*, Phys. Rev. Lett. **102**, 017205 (2009).
- [28] H. Takagi, T. Takayama, G. Jackeli, G. Khaliullin, and S. E. Nagler, *Concept and Realization of Kitaev Quantum Spin Liquids*, Nat. Rev. Phys. **1**, 264 (2019).
- [29] Y. Motome and J. Nasu, *Hunting Majorana Fermions in Kitaev Magnets*, J. Phys. Soc. Jpn. **89**, 012002 (2020).
- [30] Y. Motome, R. Sano, S. Jang, Y. Sugita, and Y. Kato, *Materials Design of Kitaev Spin Liquids Beyond the Jackeli-Khaliullin Mechanism*, J. Phys. Condens. Matter **32**, 404001 (2020).
- [31] S. Trebst and C. Hickey, *Kitaev Materials*, Phys. Rep. **950**, 1 (2022).
- [32] Y. Singh and P. Gegenwart, *Antiferromagnetic Mott Insulating State in Single Crystals of the Honeycomb Lattice Material Na_2IrO_3* , Phys. Rev. B **82**, 064412 (2010).
- [33] Y. Singh, S. Manni, J. Reuther, T. Berlijn, R. Thomale, W. Ku, S. Trebst, and P. Gegenwart, *Relevance of the Heisenberg-Kitaev Model for the Honeycomb Lattice Iridates A_2IrO_3* , Phys. Rev. Lett. **108**, 127203 (2012).
- [34] R. Comin, G. Levy, B. Ludbrook, Z.-H. Zhu, C. N. Veenstra, J. A. Rosen, Y. Singh, P. Gegenwart, D. Stricker, J. N. Hancock, D. van der Marel, I. S. Elfimov, and A. Damascelli, *Na_2IrO_3 as a Novel Relativistic Mott Insulator with a 340 meV Gap*, Phys. Rev. Lett. **109**, 266406 (2012).
- [35] C. H. Sohn, H.-S. Kim, T. F. Qi, D. W. Jeong, H. J. Park, H. K. Yoo, H. H. Kim, J.-Y. Kim, T. D. Kang, D.-Y. Cho, G. Cao, J. Yu, S. J. Moon, and T. W. Noh, *Mixing between $J_{\text{eff}} = \frac{1}{2}$ and $\frac{3}{2}$ Orbitals in Na_2IrO_3 : A Spectroscopic and Density Functional Calculation Study*, Phys. Rev. B **88**, 085125 (2013).
- [36] S. Hwan Chun, J.-W. Kim, J. Kim, H. Zheng, C. C. Stoumpos, C. Malliakas, J. Mitchell, K. Mehlawat, Y. Singh, Y. Choi, et al., *Direct Evidence for Dominant Bond-Directional Interactions in a Honeycomb Lattice Iridate Na_2IrO_3* , Nat. Phys. **11**, 462 (2015).
- [37] S. D. Das, S. Kundu, Z. Zhu, E. Mun, R. D. McDonald, G. Li, L. Balicas, A. McCollam, G. Cao, J. G. Rau, H.-Y. Kee, V. Tripathi, and S. E. Sebastian, *Magnetic Anisotropy of the Alkali Iridate Na_2IrO_3 at High Magnetic Fields: Evidence for Strong Ferromagnetic Kitaev Correlations*, Phys. Rev. B **99**, 081101 (2019).
- [38] H. Zhao, B. Hu, F. Ye, M. Lee, P. Schlottmann, and G. Cao, *Ground State in Proximity to a Possible Kitaev Spin Liquid: The Undistorted Honeycomb Iridate Na_xIrO_3 ($0.60 \leq x \leq 0.80$)*, Phys. Rev. B **104**, L041108 (2021).
- [39] K. W. Plumb, J. P. Clancy, L. J. Sandilands, V. V. Shankar, Y. F. Hu, K. S. Burch, H.-Y. Kee, and Y.-J. Kim, *$\alpha\text{-RuCl}_3$: A Spin-Orbit Assisted Mott Insulator on a Honeycomb Lattice*, Phys. Rev. B **90**, 041112 (2014).
- [40] Y. Kubota, H. Tanaka, T. Ono, Y. Narumi, and K. Kindo, *Successive Magnetic Phase Transitions in $\alpha\text{-RuCl}_3$: XY-like Frustrated Magnet on the Honeycomb Lattice*, Phys. Rev. B **91**, 094422 (2015).
- [41] L. J. Sandilands, Y. Tian, K. W. Plumb, Y.-J. Kim, and K. S. Burch, *Scattering Continuum and Possible Fractionalized Excitations in $\alpha\text{-RuCl}_3$* , Phys. Rev. Lett. **114**, 147201 (2015).
- [42] A. Koitzsch, C. Habenicht, E. Müller, M. Knupfer, B. Büchner, H. C. Kandpal, J. van den Brink, D. Nowak, A. Isaeva, and T. Doert, *J_{eff} Description of the Honeycomb Mott Insulator $\alpha\text{-RuCl}_3$* , Phys. Rev. Lett. **117**, 126403 (2016).
- [43] S. Sinn, C. H. Kim, B. H. Kim, K. D. Lee, C. J. Won, J. S. Oh, M. Han, Y. J. Chang, N. Hur, H. Sato, et al., *Electronic Structure of the Kitaev Material $\alpha\text{-RuCl}_3$ Probed by Photoemission and Inverse Photoemission Spectroscopies*, Sci. Rep. **6**, 39544 (2016).
- [44] S.-H. Do, S.-Y. Park, J. Yoshitake, J. Nasu, Y. Motome, Y. S. Kwon, D. Adroja, D. Voneshen, K. Kim, T.-H. Jang, et al., *Majorana Fermions in the Kitaev Quantum Spin System $\alpha\text{-RuCl}_3$* , Nat. Phys. **13**, 1079 (2017).
- [45] Y. Kasahara, T. Ohnishi, Y. Mizukami, O. Tanaka, S. Ma, K. Sugii, N. Kurita, H. Tanaka, J. Nasu, Y. Motome, et al., *Majorana Quantization and Half-Integer Thermal Quantum Hall Effect in a Kitaev Spin Liquid*, Nature **559**, 227 (2018).
- [46] H. Suzuki, H. Liu, J. Bertinshaw, K. Ueda, H. Kim, S. Laha, D. Weber, Z. Yang, L. Wang, H. Takahashi, et al., *Proximate Ferromagnetic State in the Kitaev Model Material $\alpha\text{-RuCl}_3$* , Nat. Commun. **12**, 4512 (2021).
- [47] R. Sano, Y. Kato, and Y. Motome, *Kitaev-Heisenberg Hamiltonian for High-Spin d^7 Mott Insulators*, Phys. Rev. B **97**, 014408 (2018).
- [48] H. Liu and G. Khaliullin, *Pseudospin Exchange Interactions in d^7 Cobalt Compounds: Possible Realization of the Kitaev Model*, Phys. Rev. B **97**, 014407 (2018).
- [49] R. Jang, Seong-Hoon and, Y. Kato, and Y. Motome, *Antiferromagnetic Kitaev Interaction in f -Electron Based Honeycomb Magnets*, Phys. Rev. B **99**, 241106 (2019).
- [50] S.-H. Jang, R. Sano, Y. Kato, and Y. Motome, *Computational Design of f -Electron Kitaev Magnets: Honeycomb and Hyperhoneycomb Compounds A_2PrO_3 ($A = \text{Alkali Metals}$)*, Phys. Rev. Mater. **4**, 104420 (2020).
- [51] Y. Sugita, Y. Kato, and Y. Motome, *Antiferromagnetic Kitaev Interactions in Polar Spin-Orbit Mott Insulators*, Phys. Rev. B **101**, 100410 (2020).
- [52] S. Biswas, Y. Li, S. M. Winter, J. Knolle, and R. Valentí, *Electronic Properties of $\alpha\text{-RuCl}_3$ in Proximity to Graphene*, Phys. Rev. Lett. **123**, 237201 (2019).
- [53] S. Mandal, D. Mallick, A. Banerjee, R. Ganesan, and P. S. Anil Kumar, *Evidence of Charge Transfer in Three-Dimensional Topological Insulator/Antiferromagnetic Mott Insulator $\text{Bi}_1\text{Sb}_1\text{Te}_{1.5}\text{Se}_{1.5}/\alpha\text{-RuCl}_3$ Heterostructures*, Phys. Rev. B **107**, 245418 (2023).
- [54] K. Miura, K. Fujiwara, K. Nakayama, R. Ishikawa, N. Shibata, and A. Tsukazaki, *Stabilization of A Honeycomb Lattice of IrO_6 Octahedra by Formation of Ilmenite-Type Superlattices in MnTiO_3* , Commun. Mater. **1**, 55 (2020).

- [55] B. Kang, M. Park, S. Song, S. Noh, D. Choe, M. Kong, M. Kim, C. Seo, E. K. Ko, G. Yi, J.-W. Yoo, S. Park, J. M. Ok, and C. Sohn, *Honeycomb Oxide Heterostructure as a Candidate Host for A Kitaev Quantum Spin Liquid*, Phys. Rev. B **107**, 075103 (2023).
- [56] Y. Haraguchi, C. Michioka, A. Matsuo, K. Kindo, H. Ueda, and K. Yoshimura, *Magnetic Ordering with an XY-like Anisotropy in the Honeycomb Lattice Iridates ZnIrO_3 and MgIrO_3 Synthesized via a Metathesis Reaction*, Phys. Rev. Mater. **2**, 054411 (2018).
- [57] S.-H. Jang and Y. Motome, *Electronic and Magnetic Properties of Iridium Ilmenites AlrO_3 ($A = \text{Mg, Zn, and Mn}$)*, Phys. Rev. Mater. **5**, 104409 (2021).
- [58] X. Hao, H. Jiang, R. Cui, X. Zhang, K. Sun, and Y. Xu, *Electronic and Magnetic Properties of Spin-Orbit-Entangled Honeycomb Lattice Iridates MlrO_3 ($M = \text{Cd, Zn, and Mg}$)*, Inorg. Chem. **61**, 15007 (2022).
- [59] K. Momma and F. Izumi, *VESTA 3 for Three-Dimensional Visualization of Crystal, Volumetric and Morphology Data*, J. Appl. Crystallogr. **44**, 1272 (2011).
- [60] P. Giannozzi, S. Baroni, N. Bonini, M. Calandra, R. Car, C. Cavazzoni, D. Ceresoli, G. L. Chiarotti, M. Cococcioni, I. Dabo, et al., *QUANTUM ESPRESSO: A Modular and Open-Source Software Project for Quantum Simulations of Materials*, J. Phys.: Condens. Matter **21**, 395502 (2009).
- [61] P. Hohenberg and W. Kohn, *Inhomogeneous Electron Gas*, Phys. Rev. **136**, B864 (1964).
- [62] J. P. Perdew and A. Zunger, *Self-Interaction Correction to Density-Functional Approximations for Many-Electron Systems*, Phys. Rev. B **23**, 5048 (1981).
- [63] P. E. Blöchl, *Projector Augmented-Wave Method*, Phys. Rev. B **50**, 17953 (1994).
- [64] A. Dal Corso, *Pseudopotentials Periodic Table: From H to Pu*, Comput. Mater. Sci. **95**, 337 (2014).
- [65] H. J. Monkhorst and J. D. Pack, *Special Points for Brillouin-Zone Integrations*, Phys. Rev. B **13**, 5188 (1976).
- [66] A. I. Liechtenstein, V. I. Anisimov, and J. Zaanen, *Density-Functional Theory and Strong Interactions: Orbital Ordering in Mott-Hubbard Insulators*, Phys. Rev. B **52**, R5467 (1995).
- [67] B. L. Chittari, Y. Park, D. Lee, M. Han, A. H. MacDonald, E. Hwang, and J. Jung, *Electronic and Magnetic Properties of Single-Layer MPX_3 Metal Phosphorous Trichalcogenides*, Phys. Rev. B **94**, 184428 (2016).
- [68] M. Arruabarrena, A. Leonardo, M. Rodriguez-Vega, G. A. Fiete, and A. Ayuela, *Out-of-Plane Magnetic Anisotropy in Bulk Ilmenite CoTiO_3* , Phys. Rev. B **105**, 144425 (2022).
- [69] A. A. Mostofi, J. R. Yates, G. Pizzi, Y.-S. Lee, I. Souza, D. Vanderbilt, and N. Marzari, *An Updated Version of Wannier90: A Tool for Obtaining Maximally-Localised Wannier Functions*, Comput. Phys. Commun. **185**, 2309 (2014).
- [70] Y. Yamaji, Y. Nomura, M. Kurita, R. Arita, and M. Imada, *First-Principles Study of the Honeycomb-Lattice Iridates Na_2IrO_3 in the Presence of Strong Spin-Orbit Interaction and Electron Correlations*, Phys. Rev. Lett. **113**, 107201 (2014).
- [71] B. H. Kim, G. Khaliullin, and B. I. Min, *Electronic Excitations in the Edge-Shared Relativistic Mott Insulator: Na_2IrO_3* , Phys. Rev. B **89**, 081109 (2014).
- [72] A. M. Oleś, *Antiferromagnetism and Correlation of Electrons in Transition Metals*, Phys. Rev. B **28**, 327 (1983).
- [73] L. M. Roth, *Simple Narrow-Band Model of Ferromagnetism Due to Intra-Atomic Exchange*, Phys. Rev. **149**, 306 (1966).
- [74] G. Khaliullin, *Orbital Order and Fluctuations in Mott Insulators*, Prog. Theor. Phys. Suppl. **160**, 155 (2005), <https://academic.oup.com/ptps/article-pdf/doi/10.1143/PTPS.160.155/5162453/160-155.pdf>.
- [75] G. Shirane, S. J. Pickart, and Y. Ishikawa, *Neutron Diffraction Study of Antiferromagnetic MnTiO_3 and NiTiO_3* , J. Phys. Soc. Japan **14**, 1352 (1959).
- [76] R. Newnham, J. Fang, and R. Santoro, *Crystal Structure and Magnetic Properties of CoTiO_3* , Acta Crystallogr. **17**, 240 (1964).
- [77] A. I. Liechtenstein, M. Katsnelson, V. Antropov, and V. Gubanov, *Local Spin Density Functional Approach to the Theory of Exchange Interactions in Ferromagnetic Metals and Alloys*, J. Magn. Magn. Mater. **67**, 65 (1987).
- [78] X. He, N. Helbig, M. J. Verstraete, and E. Bousquet, *TB2J: A Python Package for Computing Magnetic Interaction Parameters*, Comput. Phys. Commun. **264**, 107938 (2021).
- [79] J. G. Rau, E. K.-H. Lee, and H.-Y. Kee, *Generic Spin Model for the Honeycomb Iridates beyond the Kitaev Limit*, Phys. Rev. Lett. **112**, 077204 (2014).
- [80] J. Rusnačko, D. Gotfryd, and J. c. v. Chaloupka, *Kitaev-like Honeycomb Magnets: Global Phase Behavior and Emergent Effective Models*, Phys. Rev. B **99**, 064425 (2019).
- [81] M. Hanawa, Y. Muraoka, T. Tayama, T. Sakakibara, J. Yamaura, and Z. Hiroi, *Superconductivity at 1 K in $\text{Cd}_2\text{Re}_2\text{O}_7$* , Phys. Rev. Lett. **87**, 187001 (2001).
- [82] K. Ohgushi, J.-i. Yamaura, M. Ichihara, Y. Kiuchi, T. Tayama, T. Sakakibara, H. Gotou, T. Yagi, and Y. Ueda, *Structural and Electronic Properties of Pyrochlore-Type $\text{A}_2\text{Re}_2\text{O}_7$ ($A = \text{Ca, Cd, and Pb}$)*, Phys. Rev. B **83**, 125103 (2011).
- [83] J. Harter, Z. Zhao, J.-Q. Yan, D. Mandrus, and D. Hsieh, *A Parity-Breaking Electronic Nematic Phase Transition in the Spin-Orbit Coupled Metal $\text{Cd}_2\text{Re}_2\text{O}_7$* , Science **356**, 295 (2017).
- [84] Z. Hiroi, J.-i. Yamaura, T. C. Kobayashi, Y. Matsubayashi, and D. Hirai, *Pyrochlore Oxide Superconductor $\text{Cd}_2\text{Re}_2\text{O}_7$ Revisited*, J. Phys. Soc. Jpn. **87**, 024702 (2018).
- [85] S. Tajima, D. Hirai, T. Yajima, D. Nishio-Hamane, Y. Matsubayashi, and Z. Hiroi, *Spin-Orbit-Coupled Metal Candidate PbRe_2O_6* , J. Solid. State. Chem. **288**, 121359 (2020).
- [86] R. Chari, R. Moessner, and J. G. Rau, *Magnetoelectric Generation of a Majorana-Fermi Surface in Kitaev's Honeycomb Model*, Phys. Rev. B **103**, 134444 (2021).
- [87] K. Nakazawa, Y. Kato, and Y. Motome, *Asymmetric Modulation of Majorana Excitation Spectra and Nonreciprocal Thermal Transport in the Kitaev Spin Liquid Under a Staggered Magnetic Field*, Phys. Rev. B **105**, 165152 (2022).
- [88] P. W. Anderson, *The Resonating Valence Bond State in La_2CuO_4 and Superconductivity*, Science **235**, 1196 (1987).

- [89] P. A. Lee, N. Nagaosa, and X.-G. Wen, *Doping a Mott Insulator: Physics of High-Temperature Superconductivity*, Rev. Mod. Phys. **78**, 17 (2006).
- [90] J. G. Bednorz and K. A. Müller, *Possible High T_c Superconductivity in the Ba-La-Cu-O System*, Z. Phys. B **64**, 189 (1986).
- [91] P. W. Anderson, G. Baskaran, Z. Zou, and T. Hsu, *Resonating-Valence-Bond Theory of Phase Transitions and Superconductivity in La_2CuO_4 -Based Compounds*, Phys. Rev. Lett. **58**, 2790 (1987).
- [92] H. Watanabe, T. Shirakawa, and S. Yunoki, *Monte Carlo Study of an Unconventional Superconducting Phase in Iridium Oxide $J_{\text{eff}}=1/2$ Mott Insulators Induced by Carrier Doping*, Phys. Rev. Lett. **110**, 027002 (2013).
- [93] Y. J. Yan, M. Q. Ren, H. C. Xu, B. P. Xie, R. Tao, H. Y. Choi, N. Lee, Y. J. Choi, T. Zhang, and D. L. Feng, *Electron-Doped Sr_2IrO_4 : An Analogue of Hole-Doped Cuprate Superconductors Demonstrated by Scanning Tunneling Microscopy*, Phys. Rev. X **5**, 041018 (2015).
- [94] Y.-Z. You, I. Kimchi, and A. Vishwanath, *Doping a Spin-orbit Mott Insulator: Topological Superconductivity from the Kitaev-Heisenberg Model and Possible Application to $(\text{Na}_2/\text{Li}_2)\text{IrO}_3$* , Phys. Rev. B **86**, 085145 (2012).
- [95] T. Hyart, A. R. Wright, G. Khaliullin, and B. Rosenow, *Competition between d -Wave and Topological p -Wave Superconducting Phases in the Doped Kitaev-Heisenberg Model*, Phys. Rev. B **85**, 140510 (2012).
- [96] S. Okamoto, *Global Phase Diagram of a Doped Kitaev-Heisenberg Model*, Phys. Rev. B **87**, 064508 (2013).
- [97] J. Schmidt, D. D. Scherer, and A. M. Black-Schaffer, *Topological Superconductivity in the Extended Kitaev-Heisenberg Model*, Phys. Rev. B **97**, 014504 (2018).
- [98] Y. Ishikawa and S.-i. Akimoto, *Magnetic Properties of the FeTiO_3 - Fe_2O_3 Solid Solution Series*, J. Phys. Soc. Japan **12**, 1083 (1957).
- [99] H. Kato, M. Yamada, H. Yamauchi, H. Hiroyoshi, H. Takei, and H. Watanabe, *Metamagnetic Phase Transitions in FeTiO_3* , J. Phys. Soc. Japan **51**, 1769 (1982).
- [100] B. Yuan, I. Khait, G.-J. Shu, F. C. Chou, M. B. Stone, J. P. Clancy, A. Paramekanti, and Y.-J. Kim, *Dirac Magnons in a Honeycomb Lattice Quantum XY Magnet CoTiO_3* , Phys. Rev. X **10**, 011062 (2020).
- [101] B. A. Wechsler and C. T. Prewitt, *Crystal Structure of Ilmenite (FeTiO_3) at High Temperature and at High Pressure*, Am. Mineral. **69**, 176 (1984).
- [102] A. Raghavender, N. H. Hong, K. J. Lee, M.-H. Jung, Z. Skoko, M. Vasilevskiy, M. Cerqueira, and A. Samantilleke, *Nano-Ilmenite FeTiO_3 : Synthesis and Characterization*, J. Magn. Magn. Mater. **331**, 129 (2013).
- [103] H. Yamauchi, H. Hiroyoshi, M. Yamada, H. Watanabe, and H. Takei, *Spin Flopping in MnTiO_3* , J. Magn. Magn. Mater. **31**, 1071 (1983).
- [104] J. Ko and C. T. Prewitt, *High-Pressure Phase Transition in MnTiO_3 from the Ilmenite to the LiNbO_3 Structure*, Phys. Chem. Miner. **15**, 355 (1988).
- [105] N. Mufti, G. R. Blake, M. Mostovoy, S. Riyadi, A. A. Nugroho, and T. T. M. Palstra, *Magnetoelectric Coupling in MnTiO_3* , Phys. Rev. B **83**, 104416 (2011).
- [106] Y. Ishikawa and S. Sawada, *The Study on Substances Having the Ilmenite Structure I. Physical Properties of Synthesized FeTiO_3 and NiTiO_3 Ceramics*, J. Phys. Soc. Jpn. **11**, 496 (1956).
- [107] Y. Ishikawa and S.-i. Akimoto, *Magnetic Property and Crystal Chemistry of Ilmenite (MeTiO_3) and Hematite ($\alpha\text{Fe}_2\text{O}_3$) System I. Crystal Chemistry*, J. Phys. Soc. Jpn. **13**, 1110 (1958).
- [108] T. Acharya and R. Choudhary, *Structural, Dielectric and Impedance Characteristics of CoTiO_3* , Mater. Chem. Phys. **177**, 131 (2016).
- [109] B. Yuan, I. Khait, G.-J. Shu, F. Chou, M. Stone, J. Clancy, A. Paramekanti, and Y.-J. Kim, *Dirac Magnons in a Honeycomb Lattice Quantum XY Magnet CoTiO_3* , Physical Review X **10**, 011062 (2020).
- [110] G. S. Heller, J. J. Stickler, S. Kern, and A. Wold, *Antiferromagnetism in NiTiO_3* , J. Appl. Phys. **34**, 1033 (1963).
- [111] J. K. Harada, L. Balhorn, J. Hazi, M. C. Kemei, and R. Seshadri, *Magnetodielectric Coupling in the Ilmenites MTiO_3 ($M = \text{Co}, \text{Ni}$)*, Phys. Rev. B **93**, 104404 (2016).
- [112] H. Gretarsson, J. P. Clancy, X. Liu, J. P. Hill, E. Bozin, Y. Singh, S. Manni, P. Gegenwart, J. Kim, A. H. Said, D. Casa, T. Gog, M. H. Upton, H.-S. Kim, J. Yu, V. M. Katukuri, L. Hozoi, J. van den Brink, and Y.-J. Kim, *Crystal-Field Splitting and Correlation Effect on the Electronic Structure of A_2IrO_3* , Phys. Rev. Lett. **110**, 076402 (2013).
- [113] X. Zhou, H. Li, J. A. Waugh, S. Parham, H.-S. Kim, J. A. Sears, A. Gomes, H.-Y. Kee, Y.-J. Kim, and D. S. Dessau, *Angle-Resolved Photoemission Study of the Kitaev Candidate α - RuCl_3* , Phys. Rev. B **94**, 161106 (2016).
- [114] J. Knolle, D. L. Kovrizhin, J. T. Chalker, and R. Moessner, *Dynamics of a Two-Dimensional Quantum Spin Liquid: Signatures of Emergent Majorana Fermions and Fluxes*, Phys. Rev. Lett. **112**, 207203 (2014).
- [115] J. Knolle, D. L. Kovrizhin, J. T. Chalker, and R. Moessner, *Dynamics of Fractionalization in Quantum Spin Liquids*, Phys. Rev. B **92**, 115127 (2015).
- [116] A. Banerjee, C. Bridges, J.-Q. Yan, A. Aczel, L. Li, M. Stone, G. Granroth, M. Lumsden, Y. Yiu, J. Knolle, et al., *Proximate Kitaev Quantum Spin Liquid Behaviour in a Honeycomb Magnet*, Nat. Mater. **15**, 733 (2016).
- [117] J. Yoshitake, J. Nasu, and Y. Motome, *Fractional Spin Fluctuations as a Precursor of Quantum Spin Liquids: Majorana Dynamical Mean-Field Study for the Kitaev Model*, Phys. Rev. Lett. **117**, 157203 (2016).
- [118] J. Yoshitake, J. Nasu, Y. Kato, and Y. Motome, *Majorana Dynamical Mean-Field Study of Spin Dynamics at Finite Temperatures in the Honeycomb Kitaev Model*, Phys. Rev. B **96**, 024438 (2017).
- [119] J. Yoshitake, J. Nasu, and Y. Motome, *Temperature Evolution of Spin Dynamics in Two- and Three-dimensional Kitaev Models: Influence of Fluctuating Z_2 flux*, Phys. Rev. B **96**, 064433 (2017).
- [120] J. Nasu, J. Yoshitake, and Y. Motome, *Thermal Transport in the Kitaev Model*, Phys. Rev. Lett. **119**, 127204 (2017).
- [121] T. Yokoi, S. Ma, Y. Kasahara, S. Kasahara, T. Shibauchi, N. Kurita, H. Tanaka, J. Nasu, Y. Motome, C. Hickey, et al., *Half-Integer Quantized Anomalous Thermal Hall effect in the Kitaev Material Candidate α - RuCl_3* , Science **373**, 568 (2021).
- [122] L. E. Chern, E. Z. Zhang, and Y. B. Kim, *Sign Structure of Thermal Hall Conductivity and Topological Magnons*

- for *In-Plane Field Polarized Kitaev Magnets*, Phys. Rev. Lett. **126**, 147201 (2021).
- [123] J. Nasu, J. Knolle, D. L. Kovrizhin, Y. Motome, and R. Moessner, *Fermionic Response from Fractionalization in an Insulating Two-Dimensional Magnet*, Nat. Phys. **12**, 912 (2016).
- [124] A. Glamazda, P. Lemmens, S.-H. Do, Y. Choi, and K.-Y. Choi, *Raman Spectroscopic Signature of Fractionalized Excitations in the Harmonic-Honeycomb Iridates β - and γ -Li₂IrO₃*, Nat. Commun. **7**, 12286 (2016).
- [125] B. Zhou, Y. Wang, G. B. Osterhoudt, P. Lampen-Kelley, D. Mandrus, R. He, K. S. Burch, and E. A. Henriksen, *Possible Structural Transformation and Enhanced Magnetic Fluctuations in Exfoliated α -RuCl₃*, J. Phys. Chem. Solids **128**, 291 (2019).
- [126] J.-H. Lee, Y. Choi, S.-H. Do, B. H. Kim, M.-J. Seong, and K.-Y. Choi, *Multiple Spin-Orbit Excitons in α -RuCl₃ from Bulk to Atomically Thin Layers*, npj Quantum Mater. **6**, 43 (2021).
- [127] J. Feldmeier, W. Natori, M. Knap, and J. Knolle, *Local Probes for Charge-Neutral Edge States in Two-Dimensional Quantum Magnets*, Phys. Rev. B **102**, 134423 (2020).
- [128] R. G. Pereira and R. Egger, *Electrical Access to Ising Anyons in Kitaev Spin Liquids*, Phys. Rev. Lett. **125**, 227202 (2020).
- [129] E. J. König, M. T. Randeria, and B. Jäck, *Tunneling Spectroscopy of Quantum Spin Liquids*, Phys. Rev. Lett. **125**, 267206 (2020).
- [130] M. Udagawa, S. Takayoshi, and T. Oka, *Scanning Tunneling Microscopy as a Single Majorana Detector of Kitaev's Chiral Spin Liquid*, Phys. Rev. Lett. **126**, 127201 (2021).
- [131] T. Bauer, L. R. D. Freitas, R. G. Pereira, and R. Egger, *Scanning Tunneling Spectroscopy of Majorana Zero Modes in a Kitaev Spin Liquid*, Phys. Rev. B **107**, 054432 (2023).
- [132] Y. Kato, J. Nasu, M. Sato, T. Okubo, T. Misawa, and Y. Motome, *Spin Seebeck Effect as a Probe for Majorana Fermions in Kitaev Spin Liquids*, arXiv preprint arXiv:2401.13175 (2024).